

Performance of the CMS Level-1 trigger during commissioning with cosmic ray muons and LHC beams

This article has been downloaded from IOPscience. Please scroll down to see the full text article.

2010 JINST 5 T03002

(<http://iopscience.iop.org/1748-0221/5/03/T03002>)

View [the table of contents for this issue](#), or go to the [journal homepage](#) for more

Download details:

IP Address: 193.190.193.1

The article was downloaded on 28/01/2011 at 13:42

Please note that [terms and conditions apply](#).

COMMISSIONING OF THE CMS EXPERIMENT WITH COSMIC RAYS

Performance of the CMS Level-1 trigger during commissioning with cosmic ray muons and LHC beams

CMS Collaboration

ABSTRACT: The CMS Level-1 trigger was used to select cosmic ray muons and LHC beam events during data-taking runs in 2008, and to estimate the level of detector noise. This paper describes the trigger components used, the algorithms that were executed, and the trigger synchronisation. Using data from extended cosmic ray runs, the muon, electron/photon, and jet triggers have been validated, and their performance evaluated. Efficiencies were found to be high, resolutions were found to be good, and rates as expected.

KEYWORDS: Trigger concepts and systems (hardware and software); Trigger algorithms

ARXIV EPRINT: [0911.5422](https://arxiv.org/abs/0911.5422)

Contents

1	Introduction	1
2	CMS Level-1 trigger	2
2.1	Muon triggers	2
2.1.1	DT trigger	3
2.1.2	CSC trigger	3
2.1.3	RPC trigger	4
2.1.4	Global Muon Trigger	5
2.2	Calorimeter triggers	5
2.2.1	ECAL trigger primitives	5
2.2.2	HCAL trigger primitives	6
2.2.3	Regional calorimeter trigger	6
2.2.4	Global calorimeter trigger	7
2.3	Global trigger	7
2.4	Trigger software and operation	8
3	L1 trigger during CRAFT and LHC single beam operations	8
3.1	Muon triggers	8
3.2	Calorimeter triggers	9
3.3	Global triggers	10
4	Synchronisation	11
4.1	DT synchronisation	11
4.2	CSC synchronisation	12
4.3	RPC synchronisation	14
4.4	Calorimeter synchronisation	14
4.5	Global synchronisation	14
4.6	Synchronisation with LHC beam	15
5	Hardware validation using emulators	16
5.1	Muon triggers	17
5.2	Calorimeter triggers	18
6	Drift-tube trigger performance	19
7	Cathode strip chamber trigger performance	21
8	Resistive plate chamber trigger performance	24
9	Electron/photon trigger performance	26
9.1	Data selection	27
9.2	Resolution and efficiency	28

10 Jet trigger performance	29
11 Summary and outlook	31
The CMS collaboration	35

1 Introduction

The primary goal of the Compact Muon Solenoid (CMS)¹ experiment [1] is to explore particle physics at the TeV energy scale exploiting the proton-proton collisions delivered by the Large Hadron Collider (LHC) [2]. During October-November 2008 the CMS collaboration conducted a month-long data taking exercise, known as the Cosmic Run At Four Tesla (CRAFT), with the goal of commissioning the experiment for extended operation [3]. With all installed detector systems participating, CMS recorded 270 Million cosmic ray triggered events with the solenoid at its nominal axial field strength of 3.8 T. Prior to CRAFT, in September 2008, CMS observed the muon halo from single circulating beams and received several single shot “beam splash” events. In a beam splash event, the beam is steered onto closed collimators upstream of CMS, releasing $\mathcal{O}(10^5)$ muons that produce signals in most channels of the detector.

A detailed description of the CMS detector can be found in ref. [1]. Figure 1 shows a cross-section through the detector. The central feature of the apparatus is a superconducting solenoid, of 6 m internal diameter. Within the field volume are the silicon pixel and strip trackers, the crystal electromagnetic calorimeter (ECAL) and the brass-scintillator hadron calorimeter (HCAL). Muons are measured in drift tube chambers (DT), resistive plate chambers (RPC), and cathode strip chambers (CSC), embedded in the steel return yoke. Beyond the magnet yoke endcaps are iron-quartz forward hadron calorimeters (HF). The first level (L1) of the CMS trigger system, composed of custom hardware processors, is designed to select one potentially interesting event from every thousand, in less than 1 μ s processing time, using information from the calorimeters and muon detectors. The High Level Trigger (HLT) processor farm further decreases the event rate to the order of 100 Hz, before data storage. CMS uses a right-handed coordinate system, with the origin at the nominal interaction point, the x -axis pointing to the centre of the LHC, the y -axis pointing up (perpendicular to the LHC plane), and the z -axis along the anticlockwise-beam direction. The polar angle, θ , is measured from the positive z -axis and the azimuthal angle, ϕ , is measured in the x - y plane.

The CMS L1 trigger was commissioned before and during CRAFT and the single beam operation. Overall, the L1 trigger performed well during these periods; efficiencies were high and resolutions were good. Subsequent analysis of the data has allowed the performance to be quantified, and presented in this paper. The task of commissioning such a large and complex system was challenging. The trigger hardware is described in section 2, and its use in CRAFT and LHC single beam operation are described in section 3. The results of trigger synchronisation are described in section 4. Section 5 describes the comparison of the trigger data with a software emulation of

¹A glossary of acronyms used in this paper may be found in ref. [1] p309

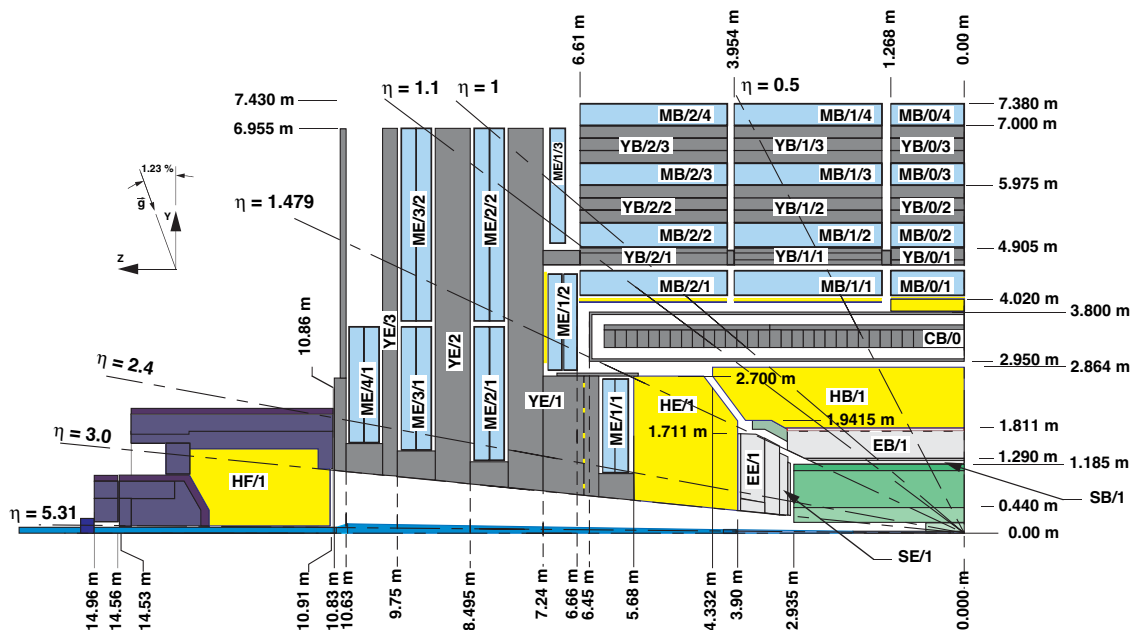


Figure 1. Cross-section through the CMS detector in the y - z plane.

the system. The performance measurements are described in sections 6–10, covering muon triggers from three subdetectors, e/γ and jet triggers. In general, these analyses use only fractions of the CRAFT dataset, because the performance is evaluated using events similar to those of LHC collisions for which the L1 trigger design was optimised.

2 CMS Level-1 trigger

The CMS L1 trigger is described in detail in ref. [4]. In brief, the calorimeters and the muon subdetectors provide trigger primitives in the form of local energy deposits in calorimeter trigger towers and track segments or hits in muon chambers. Regional and global processors identify trigger objects: electron, jet, and muon candidates, and energy sums. A full set of trigger primitives are produced every 25 ns, a period known as a “bunch-crossing” (BX). For LHC collisions, this identifies the trigger primitives and resulting trigger objects with a particular proton-proton collision. Objects are ranked and sorted. They form the basis for trigger decisions taken by the final L1 stage, the Global Trigger (GT), according to programmable algorithms. The Trigger Control System (TCS) determines if the subdetectors are ready to read out the event, and if the data acquisition (DAQ) system is ready to receive it. Data from trigger primitives, regional energy sums, muon candidates from each sub-detector, and final trigger objects are sent in parallel to the DAQ for each accepted event. Control and monitoring of the L1 trigger operation are performed centrally by dedicated software.

2.1 Muon triggers

Drift tube chambers in the barrel of the detector and cathode strip chambers in the endcap regions provide tracking up to pseudorapidity $|\eta| = 2.4$ and trigger information up to $|\eta| = 2.1$. Resistive

plate chambers cover up to $|\eta| = 1.6$ and are used mainly for triggering purposes. The chambers are mounted in the return yoke of the solenoid that is composed of five wheels in the barrel region and three disks in each of the endcaps. Wheels and disks are subdivided into azimuthal sectors covering approximately 30° or 60° (with some overlap). The DT and CSC share trigger information in the overlap region, enabling each of the three muon subdetectors to deliver its own list of up to four muon candidates, ranked and sorted according to decreasing reconstruction quality and transverse momentum, to the Global Muon Trigger (GMT) [5]. This then combines them and forwards up to four candidates to the GT.

2.1.1 DT trigger

The DT system consists of 250 “chambers” arranged in four muon stations (MB1, MB2, MB3, and MB4) embedded in the steel yoke of CMS. Each DT chamber consists of staggered planes of drift cells. Four planes form a superlayer. The three innermost stations are made of chambers with three superlayers; the inner and outer superlayers measure ϕ while the central superlayer measures η . The fourth muon station has only ϕ -superlayers.

The on-chamber electronics produce trigger primitives, consisting of information about identified track segments. They are generated separately for the “ ϕ -view” (in the $x - y$ plane) and the “ θ -view” (in the $r - z$ plane). Up to two primitives per chamber and per bunch-crossing (BX) are generated in the ϕ -view, each primitive comprising the track segment position, direction and a quality code. The latter encodes the number of drift cell hits that were found aligned by the trigger logic, labelling a primitive built with four or three hits from the four staggered layers of a superlayer, “High” (H) or “Low” (L) quality, respectively. If a proper matching, or correlation, between the segments from the two superlayers in the ϕ -view is found, the primitive is labelled HH, HL, or LL. If a proper correlation is not found, single H or L segments are output. In the θ -view, segments are accepted only if their direction is compatible with a track that originated from the interaction point. Thus, no information about direction is output, and the positions of valid segments are encoded into a bit pattern.

Trigger primitives from a given muon sector are sent to the Sector Collector electronics, located outside of the detector. The signals from each station are synchronised, coded, and forwarded through high-speed optical links [6] to the Drift Tube Track Finder (DTTF) located in the underground counting room adjacent to the detector. The DTTF also receives trigger primitives from the CSCs for the barrel-endcap overlap region. The DTTF system performs matching between trigger primitives received from the DT stations and assigns a quality code as well as ϕ , η , charge and transverse momentum (p_T) values to the reconstructed muon track. The track matching is based on extrapolation. The standard algorithms used to identify muons from LHC collisions are described in detail in ref. [7]. Different algorithms are used for cosmic ray triggers, and are described in section 3. The Sector Collector and the DTTF also read out their input and output data for several time samples around the triggered event for diagnostics and monitoring.

2.1.2 CSC trigger

The CMS endcap muon system includes 468 trapezoidal cathode strip chambers with different ϕ coverage, arranged to form four disks at each endcap (stations ME1, ME2, ME3, and ME4). Each station is in turn subdivided into rings of chambers as follows: ME1 has three rings of chambers

(ME1/n, $n=1,2,3$), ME2 and ME3 stations have two rings of chambers, and ME4 has one ring of chambers. Each chamber consists of six layers equipped with anode wires and cathode strips.

In each chamber, the track segment position, angle and bunch crossing, are first determined separately in the nearly orthogonal anode and cathode views. The cathode readout is optimised to measure the ϕ -coordinate, while the anode readout is optimised to identify the bunch crossing. The front-end electronics boards reconstruct track segments using pattern-recognition firmware based on pattern templates. These templates require track segments in cathode as well as anode views to point towards the interaction point, with an angular acceptance, of order one Radian, depending on the station. The track segments from the cathode and anode readout from each chamber are finally combined into 3-dimensional local tracks, which are the CSC trigger primitives. The trigger primitives are collected by the Muon Port Cards, which sort them and send up to three candidates to the CSC Track Finder (CSCTF) via optical fibres.

The CSCTF matches trigger primitives to form complete tracks and determine their p_T , η , ϕ and charge. The CSCTF functionality is described in more detail in ref. [8]. For the purpose of track finding, the CSC detector is logically partitioned into six 60° azimuthal sectors per endcap. The trigger primitives from each sector are received and processed by single Sector Processor boards. The CSCTF also receives trigger primitives from the DT system for the barrel-endcap overlap region. The CSCTF is optimized to cope with the non-axial magnetic field present in the endcap region. Thus, the algorithms of the CSCTF are inherently 3-dimensional to achieve maximum background rejection, in particular for low momentum tracks. In addition to the p_T , η , ϕ , and charge, each track identified by the CSCTF carries a quality code. This quality code is used along with the p_T to sort the candidates; the highest ranking four are sent to the Global Muon Trigger. The quality code is a two-bit word that is used to indicate the expected coarse p_T resolution. Quality 3 (high p_T resolution) refers to a three- or four-segment track with one of the segments in ME1. Quality 2 (medium p_T resolution) refers to a 2-segment coincidence with one of the segments in ME1. Quality 1 (low p_T resolution) refers to any other 2-segment coincidence. Quality 3 candidates, with $5 < p_T < 35 \text{ GeV}/c$, are expected to have about 20% resolution in p_T , while quality 2 are expected to have about 30%. In addition to identifying muons originating from the interaction point, the CSCTF identifies tracks from ‘‘halo muons’’, coming from the interaction of the LHC beam with the gas particles in the beam pipe or with the beam pipe itself. This set of muons, parallel to the beam line, has proven to be very useful at the LHC start-up to align the several endcap disks [9].

2.1.3 RPC trigger

In the barrel and endcap regions, the DT and CSC chambers are complemented by double-gap resistive plate chambers. The RPCs are arranged in six layers in the barrel region and three layers in the forward regions. They have excellent timing resolution, of the order of 1 ns. Their main purpose is to identify the bunch-crossing in which the detected muon was emitted. They also assign track parameters. The RPC trigger is based on the spatial and temporal coincidence of hits in several layers. The Pattern Comparator trigger logic [10] compares signals from all four muon stations to predefined hit patterns in order to find muon candidates. Muon p_T , charge, η , and ϕ are assigned according to the matched pattern. The algorithm requires a minimum number of hit planes, which varies with the p_T and location of the muon. Either 4/6 (four out of six), 4/5, 3/4 or

3/3 hit layers are minimally required. A quality value, encoded in two bits, reflects the number of hit layers. Analog signals from the chambers are digitized by Front End Boards, then zero-suppressed and assigned to the proper bunch crossing by a system of Link Boards located in the vicinity of the detector. They are then sent via optical links to Trigger Boards located in the underground counting room. Each of the 84 Trigger Boards can produce up to four muon candidates for every bunch crossing. A system of two Half-Sorter Boards followed by a Final Sorter Board sorts the candidates by quality and p_T , and sends up to eight muon candidates, four from the barrel and four from the endcaps, to the GMT.

2.1.4 Global Muon Trigger

The Global Muon Trigger receives up to 4 candidates from each of the DTTF and CSCTF and up to 8 candidates (4 in the barrel, and 4 in the endcap) from the RPC trigger. Look-up tables (LUTs) are used to combine candidates identified by more than one sub-detector, and to assign a quality code based on the number of subdetectors involved, as well as on the quality of the track candidates, as assigned by the track-finders. The four highest quality muon candidates are forwarded to the GT. The GMT also reads out its input and output data for 3 time samples around each triggered event, for diagnostics, monitoring, and to indicate regions of interest to HLT.

2.2 Calorimeter triggers

For triggering purposes the barrel and endcap calorimeters are subdivided in trigger towers. The pattern of energy deposited in those towers is analyzed to identify electron/photon and jet candidates, and the tower energies are summed to obtain the candidate transverse energy (E_T). A trigger primitive is generated for each trigger tower in the ECAL and HCAL, up to $|\eta| = 3.0$. The towers have the same segmentation in both the ECAL and HCAL. Their size is $\Delta\eta \times \Delta\phi = 0.087 \times 0.087$ in the barrel and in the endcaps up to $|\eta| = 1.8$. For $|\eta| > 1.8$, the tower segmentation in η increases to $\Delta\eta = 0.1 - 0.35$. Trigger primitives from the forward region, which covers the range $3.0 < |\eta| < 5.0$, are used for jet and energy sum triggers only. A single trigger primitive is generated for each HF trigger region, which are equal to $3\eta \times 2\phi$ readout towers, and are of constant size; $\Delta\eta \times \Delta\phi = 0.5 \times 0.349$. The initial energy scale for calorimeter triggers was derived from test beam results, and in the case of HCAL was further fine-tuned using Monte-Carlo simulations.

2.2.1 ECAL trigger primitives

The ECAL trigger primitive generation (TPG) starts in the on-detector front-end electronics after digitisation of the signal, by summing the energy from each PbWO_4 crystal in a strip of five in the ϕ direction and converting the result to E_T , taking into account the electronics gains and calibration coefficients. An amplitude filter is applied to the strip sum consisting of the weighted sum of five 25 ns time samples, taking into account the expected signal shape and residual pedestal to be dynamically subtracted. Finally, a peak finder applied to three consecutive time samples in a sliding window requires the amplitude of the central sample to be maximum, keeping this value as a measure of the transverse energy contained in the strip. The E_T values from five adjacent strips in η are then summed and the E_T estimate for the trigger tower is transferred to the Regional Calorimeter Trigger (RCT). The E_T value is encoded in 8 bits. In addition, a fine-grain veto bit is

set for each trigger tower if the highest two adjacent strips in the tower contain less than 90% of the total E_T . This gives some indication of the lateral shower shape, and can be used to reject L1 electron/photon (e/γ) candidates that result from physical jets.

2.2.2 HCAL trigger primitives

HCAL signals are digitised on-detector and the data transmitted to the HCAL trigger and readout boards via optical fibres. The TPG processing for barrel and endcap is different from the forward calorimeter, and is described first. The barrel and endcap trigger primitives are formed by first linearising the received signal, using LUTs that are programmed to account for individual channel gains and pedestals. The trigger towers are the same size in $\eta \times \phi$ as the readout towers, but energies from separate longitudinal readout channels are summed. The pulse energy is obtained by summing two adjacent 25 ns time samples and the peak time is found by a peak finder applied to three consecutive samples, as described for ECAL trigger data. The resulting energy value for the trigger tower is compressed before being sent to the RCT, using an analytical compression function that has no loss of precision at low energies and matches the calorimeter resolution at high energies. The forward calorimeter trigger primitives are generated by linearising signals from the front-end and converting to E_T , again accounting for channel gains and pedestals. These are then summed over $3\eta \times 2\phi$ towers to give a trigger region of 0.5×0.349 , which is not too large since the forward calorimeter is only used in jet and energy sum triggers. The pulses are short, so no temporal sums or peak detection are required. E_T values are sent to the RCT. A fine-grain bit, used by dedicated minimum bias triggers, is set for each HF trigger region if one or more of the 6 readout towers entering the sum has E_T above a programmable threshold.

The CMS barrel HCAL includes a “tail catcher” outside the magnet solenoid (HO). Signals from this detector are not included in the HCAL trigger primitives, but a technical trigger is generated that requires a single readout segment to be above a threshold.

2.2.3 Regional calorimeter trigger

The RCT receives the ECAL and HCAL trigger primitives in 18 electronics crates, each covering one half of the detector in z and 40° in ϕ . The RCT Receiver Cards use LUTs to decompress the HCAL values to E_T . The Electron Identification Cards then identify e/γ candidates up to $|\eta| \sim 2.5$, using a sliding window algorithm based on 3×3 trigger towers, with the central tower of the 3×3 window required to have greater E_T than its neighbours. The resulting candidates are classified as isolated or non-isolated, according to the ECAL trigger primitive fine-grain veto information, and the ratio of HCAL to ECAL E_T , calculated in the RCT [1]. The E_T of the e/γ candidate is taken as the sum of that in the central tower and its highest E_T neighbour, and a coarse position is assigned as the centre of the 4×4 tower region in which the candidate is contained. Each RCT crate transmits up to four isolated and four non-isolated e/γ candidates to the Global Calorimeter Trigger (GCT).

In addition, the Receiver Cards sum the ECAL and HCAL tower E_T values over non-overlapping 4×4 towers (for barrel and endcaps) and forward these region sums via the Jet Summary card to the GCT. For each region, the RCT sends a τ -veto bit to the GCT, which indicates that the tower energy is spread out over multiple towers, rather than contained in a small number of contiguous

towers, and hence is not consistent with a τ -lepton decay. The HF trigger regions are forwarded directly to the GCT without processing.

2.2.4 Global calorimeter trigger

The GCT hardware [11] has been completely redesigned since the L1 Trigger Technical Design Report [4], to take advantage of new technologies and improve the robustness of this complex system. The e/γ candidates and region sums are received from the RCT crates by 63 Source Cards, which serialize the data and transmit them to the main GCT crate via optical fibres. The e/γ candidates are received by two Electron Leaf cards, which sort them based on E_T , and forward the highest four isolated and highest four non-isolated candidates to the GT. Six Jet Leaf cards process the region sums, finding jets and summing E_T . Two Wheel cards, each covering a half-detector in z , then sort and select the jets, and calculate energy sums. Finally, a single Concentrator card performs final jet sorting and calculates full detector energy sums. Jet candidates are identified using a 3×3 sliding window of trigger regions (equivalent to 12×12 trigger towers, or 1.05×1.05 in $\eta \times \phi$). The jet-finder algorithm is described in detail in ref. [12]. After jets are found, LUTs are used to apply a programmable η -dependent jet energy scale correction. Jets found with $|\eta| > 3.0$ are classified as forward jets. Those found with $|\eta| < 3.0$ are classified as central or τ , depending on the OR of the nine τ -veto bits associated with the 9 regions in the 3×3 window. The GCT also calculates total and missing E_T from the trigger regions, and total and missing H_T . The total H_T is the scalar sum of E_T identified in jets, and missing H_T is the corresponding vector sum in the $x - y$ plane. Finally, minimum-bias trigger quantities are formed by summing E_T in rings around the beampipe in the HF calorimeter (for $4 < |\eta| < 4.5$ and $4.5 < |\eta| < 5$), and by counting fine-grain bits set by the HF TPG. The four highest E_T jets in each of the central, τ and forward categories are sent to the GT, along with E_T^{total} , E_T^{miss} , H_T^{total} , H_T^{miss} and the minimum-bias quantities. The GCT transmits all input and output data to the DAQ for each triggered event, to be used for diagnostics, monitoring and HLT regions of interest.

2.3 Global trigger

The main task of the Global Trigger is to reject or to accept events for readout and further processing by the high-level trigger. Before performing trigger algorithm calculations, it has to first receive and synchronise the muon and calorimeter input data. This task is achieved by several Pipelined Synchronizing Buffer (PSB) cards. The data are then transmitted to the Global Trigger Logic (GTL) board. This unit is programmed to provide a menu of up to 128 algorithms, which can transform logical combinations of L1 trigger objects (muons, jets, e/γ , calorimeter transverse energy sum, etc.) with selection criteria (energy/momentum thresholds, etc.) into decision bits. These bits can be enabled to contribute to a final OR of decisions which determines whether the data are read out. In addition, a special PSB receives up to 64 simple on/off signals, called technical triggers, that can be added to contribute to the final OR [13]. Random triggers can also be generated using a linear congruential random number generator. Input data for 3 time samples around the triggered event are read out by the GT Front-End Module (GTFE). The GT boards are housed in a single crate, which also contains the GMT and the TCS.

Besides combining and propagating triggers from subdetectors, the GT provides a throttling mechanism to assure that all triggered events can be completely recorded by the DAQ system. Part

of this mechanism is the application of programmable trigger rules, which prevent accumulation of triggers in short time intervals. The rules used are: no more than 1 trigger in 3 BX's, 2 in 25, 3 in 100, 4 in 240. Moreover, front-end buffers of subdetectors can signal to the GT that they are filling up, which results in the GT interrupting trigger activity until the buffers are emptied and the flag removed. Counters in the GT record the overall trigger rate and the individual rate of each trigger algorithm and technical trigger, as well as dead time counters that record the amount of time during which triggers were inhibited.

2.4 Trigger software and operation

The trigger system is controlled and monitored centrally, using the Trigger Supervisor [14] and XDAQ [15] software frameworks. The configuration of the trigger electronics is managed by the Trigger Supervisor, using predefined configuration conditions stored in a database. At run start, the shift personnel are able to choose the configuration of each subsystem from a list of keys provided by subsystem experts, allowing flexibility in the trigger configuration whilst also ensuring reproducibility and reducing possibility for human error. The shift personnel are also able to enable, mask, or prescale individual trigger algorithms, providing robustness against unexpected detector conditions. The configuration data and trigger masks used for each run are recorded in online databases and stored offline for use in offline analysis, such as validation of the trigger operation using emulators. During the run, shift personnel monitor the trigger system through direct monitoring of system status, via hardware registers and the GT counters described above, and through data quality monitoring histograms of the actual data recorded.

3 L1 trigger during CRAFT and LHC single beam operations

In this section, the trigger operation during CRAFT and LHC single beam periods is described, including the hardware that was operational and how the trigger was configured for cosmic rays, beam splash events, and single circulating beams.

3.1 Muon triggers

The muon trigger systems are designed to identify muons originating from the interaction point (IP) with high acceptance and efficiency. However, cosmic ray muons arrive from many directions and the vast majority that traverse the detector do not come close to the IP. As a result, the detector acceptance and/or the track segment matching efficiency is not optimal for cosmic rays. During CRAFT, the muon trigger configuration was adjusted to give the highest possible rate of cosmic ray muons.

Unlike muons from bunched beam interactions, cosmic ray muons arrive uniformly distributed in time. The DT electronics devoted to the bunch crossing identification requires a fine synchronisation to the phase of LHC collisions. Cosmic ray muons arriving at a marginal time with respect to the optimal phase can be detected as lower quality, or out of time trigger primitives. Segments reconstructed using a single superlayer, called uncorrelated triggers, were allowed only if of H type (section 2.1.1) and confirmed by a coincidence with the trigger primitives from the θ -view. Details of the DT trigger primitives configuration and performance can be found in [16].

To improve the cosmic ray muon acceptance, the DTTF extrapolation mechanism was relaxed. A track was generated if a muon in one sector, or crossing two neighbouring sectors, produced at least two trigger primitives at the same bunch-crossing (BX) in two different stations - with no requirements on their position or direction. This configuration is referred to as “open LUTs”, while the configuration used for muons originating from LHC collisions is known as “closed LUTs”. A consequence of this was that no p_T assignment to DTTF track candidates was possible.

Five DTTF modules were not operational and thus masked (7% of the system) and the internal connections to allow track finding across sector boundaries were installed but not commissioned. Finally, the link system connecting the θ -view output of the DT trigger primitive generators was not yet commissioned; as a consequence the DTTF system could only assign low-resolution η values to track candidates.

Similarly, to improve the cosmic muon acceptance, the CSCTF was operated in a mode where a muon candidate is generated from a single trigger primitive, and assigned quality 0. The CSC trigger primitives were formed using standard LHC collision pattern templates. This was performed in addition to the regular mode of operation, where muon candidates are generated from several matching trigger primitives, and assigned higher quality codes. The halo muon algorithm was operational during CRAFT and first beam. DT trigger primitives were not yet included in the CSCTF track finding in the region of the DT-CSC overlap.

For the RPC system, triggers were supplied only by the barrel. The RPC Pattern Comparator trigger electronics were fully installed and functional. The hit patterns that can be identified by the RPC trigger are constrained by the connectivity between RPC strips and the Pattern Comparator. The strips that can be compared to a given pattern template are arranged in cones radiating from the IP. To achieve good acceptance for cosmic muons, the Pattern Comparator was programmed with patterns that produce a muon candidate from the logical OR of all strips in each cone. Measurement of muon sign and p_T is not possible with these pattern template. In addition to this, the coincidence requirements were loosened by allowing the coincidence of 3 out of 6 detector layers in the barrel. Muon candidates were assigned a quality value based solely on the number of planes that fired (0 to 3, corresponding to 3 to 6 firing planes). The standard “ghost busting” algorithm [17] was applied to prevent single muons producing more than one candidate in logical cones that overlap in space. A single candidate was selected on the basis of higher quality followed by higher ϕ value.

The main function of the Global Muon Trigger during CRAFT was to synchronise triggers from the three muon systems. Another important function was to record L1 muon track candidates in a unified format in the event data such that the performance of individual muon trigger systems could be conveniently analyzed. Other functions, like smart quality assignment and cancellation or merging of duplicate candidates (described in ref. [5]) were applied but not actively used.

3.2 Calorimeter triggers

During CRAFT, the calorimeter triggers were configured to trigger on instrumental noise and energy deposited by cosmic rays. Only the ECAL barrel was used to provide e/γ triggers, since the ECAL endcap trigger electronics were not installed yet. The ECAL trigger primitive transverse energy was sent to the RCT on a linear scale, with a least significant bit (LSB) corresponding to 250 MeV, the maximum possible value being 63.75 GeV. In order to minimize the contribution from noise, trigger primitives below 750 MeV were suppressed. This value corresponds to between

three and four times the noise. HCAL was operated in the standard way for cosmic and LHC runs. For most of CRAFT, all three calorimeter parts (barrel, endcap and forward) were active. The barrel and endcap HCAL trigger primitives were sent to the RCT using an 8-bit non-linear scale in energy. The HF trigger primitives were sent on a linear transverse energy scale, with the LSB of 250 MeV.

The full Regional Calorimeter Trigger was used during CRAFT. The default RCT configuration used during cosmic ray runs produced e/γ candidates from ECAL barrel trigger primitives, and region sums from the sum of ECAL (barrel) and HCAL (barrel, endcap and forward) trigger primitives. Noisy or absent ECAL and HCAL channels were masked in the RCT LUTs. A total of 8.5% of ECAL trigger towers were masked; the number has since been reduced through finer-granularity (crystal) masks. Less than 1% of HCAL channels were masked. The RCT input LUTs were generated from the scales provided by ECAL and HCAL, to give linear E_T with a 250 MeV LSB. The isolation, “fine-grain”, and H/E criteria were ignored in the production of e/γ candidates. The e/γ candidate E_T , which is the sum of E_T in a pair of contiguous ECAL trigger towers, was transmitted to GCT (and thence to GT) on a linear scale with a LSB of 500 MeV. This algorithm is referred to as an e/γ trigger, although the requirement is simply an ECAL energy deposit above a configurable cut.

The GCT jet and e/γ trigger algorithms were enabled during CRAFT. The global energy sum and minimum-bias algorithms had not been commissioned at that time. No jet energy corrections were applied to the jet E_T . The output jet E_T scale was chosen to be linear with 2 GeV steps from zero to 126 GeV.

3.3 Global triggers

During cosmic data taking, only the simplest single object algorithms were enabled in the GT, with no threshold for muons and the lowest energy threshold allowed by the noise rate for calorimeter objects. The trigger algorithms enabled in the Global Trigger during CRAFT were:

- L1_SingleMuOpen: any muon candidate from any sub-detector with any p_T
- L1_SingleEG1: single e/γ candidate with $E_T > 1$ GeV
- L1_SingleJet10: single jet candidate with $E_T > 10$ GeV

Since the outer section of the hadron calorimeter (placed behind the magnet coil in the central part of CMS), called the HO, does not contribute to the jet trigger, a self-triggering HO technical trigger was introduced to provide insight into the noise behavior of this device, and to investigate timing.

The average rate of each of these triggers during CRAFT is given in table 1, along with the total overall rate. The DT in coincidence with the RPC trigger gave 120 Hz rate, and the CSC with the RPC trigger yielded 20 Hz. The rate of coincidence between calorimeter triggers and the single open muon trigger was: 0.5 Hz for the single e/γ trigger, 0.9 Hz for the single jet trigger, and 0.15 Hz for the HO technical trigger.

Complementary to these “physics” triggers, the GT system routinely provided calibration triggers with a rate of 100 Hz preceded by control signals used to fire calibration systems in various

Table 1. Nominal L1 trigger rates during CRAFT.

Trigger	Rate (Hz)
L1_SingleMuOpen	300
L1_SingleMuOpen (DT only)	240
L1_SingleMuOpen (RPC only)	140
L1_SingleMuOpen (CSC only)	60
L1_SingleEG1	23
L1_SingleJet10	140
HO technical trigger	14
Total	475

subdetectors. During such a calibration sequence all “physics” triggers were disabled for about 5 μ s, introducing a dead-time of 3%. Note that such calibration triggers occur during the LHC abort gap when running with beam, so this does not imply a real deadtime for LHC physics triggers. Finally, low rate Poissonian distributed random triggers were added to the trigger mix.

During LHC single beam operations in 2008, the GT was programmed to trigger on CSC beam halo muon candidates, as well as technical triggers from LHC beam pickup monitors (BPTX) and the HF detector. The BPTX system uses signals from electrostatic devices, located on the beam pipe 175 m from CMS in each direction, that produce signals synchronous with a passing proton bunch. For single circulating beams, a technical trigger is generated from the BPTX upstream of CMS. The HF technical trigger required a single tower with energy above a threshold of 15 GeV.

4 Synchronisation

For efficient triggering, all parts of the CMS detector must produce trigger signals synchronously for the same event. For LHC collisions, synchronisation to the same BX is relatively easily achieved. Synchronisation for cosmic ray muon detection, however, was more challenging. Cosmic ray muons arrive asynchronously, from all directions, and the time of flight for a relativistic particle to traverse the detector is much greater than the clock period. Despite this, the detector was well synchronised, as described in this section.

4.1 DT synchronisation

In order to provide a cosmic ray muon trigger, the behavior of the DT trigger primitives with respect to the arrival time of the muons was investigated. Cosmic rays arrive with a flat timing distribution, while the DT trigger was designed to identify the bunch crossing of muons from beam collisions. The time at which the muon crosses the chamber is computed as an additional parameter of the track segment object delivered by the offline local reconstruction [18], with a resolution of ~ 3 ns. In the left plot of figure 2, the time distribution of muons in a given chamber is shown, as well as the tracks triggered with HH quality code, at the “good” and neighbour BX respectively. HH triggers can provide a precise BX assignment, and their efficiency as a function of time was

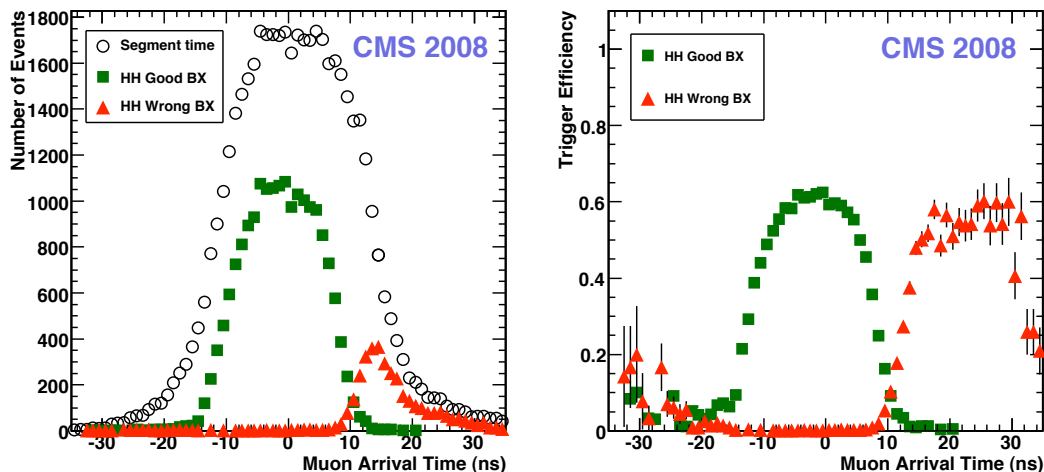


Figure 2. Distribution of the arrival time of muon track segments (*left, open circles*), and for segments which also have an associated HH local trigger in the station at the correct (*squares*) and neighbour BX (*triangles*). Ratio between the HH-triggered and all muon track segments corresponding to the HH trigger efficiency (*right*), shown for the correct (*squares*) and neighbour BX (*triangles*).

shown to be a precise indicator of the trigger synchronisation in dedicated test-beams with bunched muons [19]. The ratio of the inner and outer curves from this plot corresponds to the efficiency for HH triggering, and is shown in figure 2 (right). The HH efficiency plateau in both BX curves is about 60%, as expected for a well timed-in trigger system, while the HH efficiency decreases in the region between the two consecutive BXs. In this region, the overall efficiency is recovered by lower quality triggers, whose BX identification power is lower. This analysis of the trigger performance with respect to the muon track time has been developed as a tool in the initial process of fine synchronisation of the DT trigger to the LHC bunch crossing time [20].

The local trigger synchronisation was specifically adjusted for cosmic ray triggers. Cosmic ray muons generally cross the detector from top to bottom, so the system was synchronised to take this into account. The trigger latency of the chambers of the top sectors was increased using configurable pipelines in the Sector Collector modules, accounting for a maximum time of flight to the bottom chambers of about 50 ns, or 2 BX. Thus, when a single muon crosses two sides of the detector, two segments from different detector regions are sent to the DTF in the majority of cases for the same BX, so that the DTF system sends two muon track candidates to the GMT at the same BX.

The synchronisation parameters were obtained with dedicated runs, by means of checking the bunch crossing distribution of trigger segments from different detector regions with respect to a reference DT sector. Figure 3 shows the resulting mean BX for each of the chambers in wheel 0, which are compatible to about one third of a BX.

4.2 CSC synchronisation

For CRAFT, a coarse delay of 1 BX was introduced for the upper chambers with respect to the bottom. Precise inter-chamber synchronisation of the CSC detector is achieved by measuring the

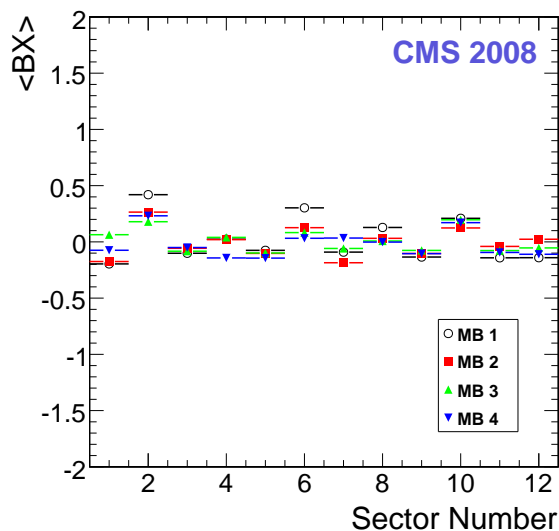


Figure 3. Mean BX from DT chambers of wheel 0.

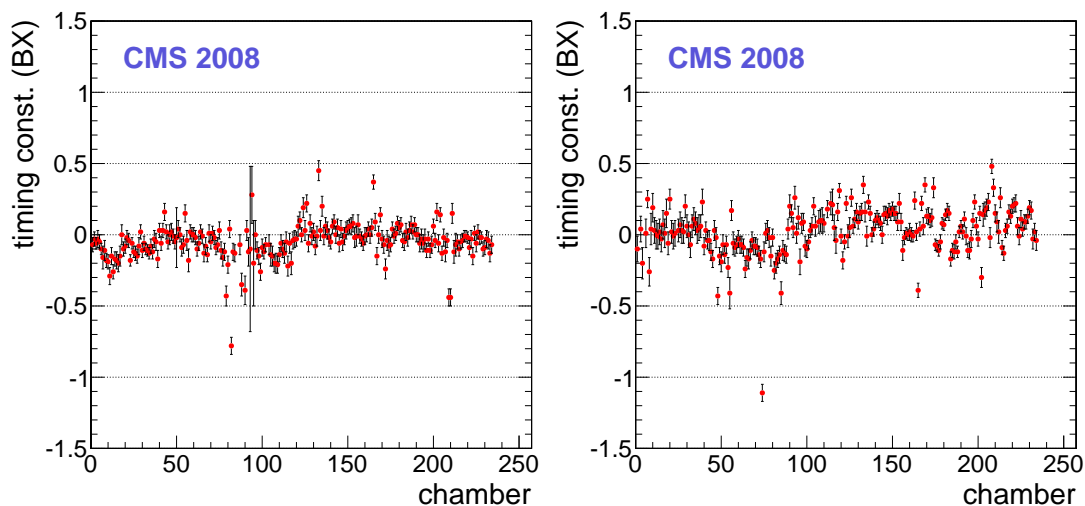


Figure 4. CSC inter-chamber timing constants from CRAFT for the plus (*left*) and minus (*right*) endcaps after adjustment of delays based on CRAFT analysis.

arrival time at the CSCTF of trigger primitives from the same event, on a chamber by chamber basis. For each endcap, the mean relative time of signal arrival in each chamber is measured relative to a single reference chamber. These measurements are used to construct a global χ^2 , minimization of which can yield optimal timing constants for each chamber simultaneously. The mean arrival time of signals from all CSC chambers, after adjustment using this method are shown in figure 4. They indicate the precision of CSC inter-chamber synchronisation achieved during CRAFT to be around 0.15 BX.

4.3 RPC synchronisation

The RPC Link Boards were synchronised such that the cosmic ray muons crossing top and bottom parts of the detector produce triggers in the same BX. The initial settings were calculated from fibre and cable lengths and assuming the time of flight to the chambers as the time to cover the distance from the outermost layer of the top barrel sector for a straight, vertical track. The distance between the chambers was computed from the detector geometry. Adjustments to these settings were obtained from dedicated data-taking runs, in which only the RPC trigger was enabled.

Distributions of the muon hit BX with respect to the BX of the trigger were produced for each Link Board and corrected timing constants were calculated. The different parts of the detector were synchronised in consecutive steps. First, the corrections for the Link Board of the bottom sector of wheel 0 were found, based on data in which triggers coming only from that sector were enabled. In the next run, again only triggers from the bottom sector of wheel 0 were enabled, and used as a reference for the top sectors of wheels -1, 0, 1. In a similar way, the other parts of the detector were synchronised; the corrections for the bottom sectors of wheels -1, 0, 1 were calculated with respect to the muons triggered in the top sector of wheel 0, the top sectors of wheels -2 and 2 were synchronised with respect to the bottom sector of wheels -1 and 1, and so on up to the endcap. More details can be found in ref. [21].

4.4 Calorimeter synchronisation

The ECAL trigger primitives were synchronised by measuring the signal arrival time in DT-triggered events. Ten time samples were read out, and the signal peak was required to be in the 6th 25 ns time sample. Initial delays for each channel were set according to fibre length from the detector. No additional channel by channel synchronisation was required.

The sampling phase of each HCAL channel was individually adjusted to compensate for differences in particle time of flight from the interaction point, and signal propagation delays in the scintillator tile fibres. These delays were determined in the test beam, and validated using the beam splash events. Laser test pulses distributed to most portions of the detector were also used to check the synchronisation. These methods demonstrate that the HCAL sampling had an RMS variation of 2 ns during CRAFT. In addition to the uniformity of sampling phase, it is possible that the digitized samples shift latency by 1 BX during their transfer from the front ends to the HCAL trigger/readout cards. During CRAFT, the system of optical latency control was still imperfect, and about 0.2% of the data was shifted by 1 BX. Measures have been taken since CRAFT to correct this.

4.5 Global synchronisation

After each of the three muon systems was internally synchronised, it was necessary to make sure that the signal created by the same muon in different detectors enters the GMT in the same clock cycle. With cosmic rays, this is only possible to a limited extent, depending on the level of internal subdetector synchronisation. Using latency calculations of upstream trigger pipelines, it was possible to determine rough delay settings at the GMT inputs. Fine tuning of these delays was then performed using the cosmic ray data. One method is to measure the signal arrival time from a particular subdetector with respect to triggers from another. A direct comparison is possible using the readout of the GMT, which records all input muon candidates and reads 3 consecutive clock

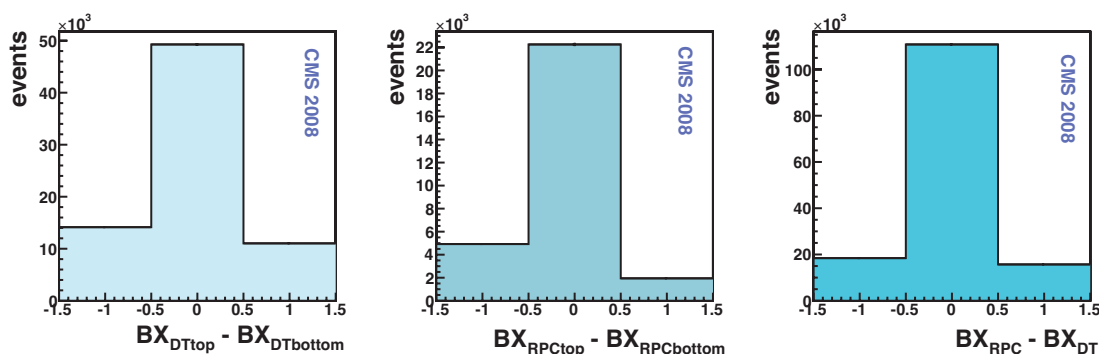


Figure 5. Time differences at the GMT in terms of BX between L1 muon candidates - created in most cases by the same cosmic ray muon - from the top half and the bottom half of the DT system (*left*) and the RPC (*middle*) and between the RPC and DT system (*right*). The majority of the signals are synchronised and the skew at the clock edges is balanced.

cycles centered at the trigger. Figures 5 and 6 show that in most cases L1 muon candidates from different muon systems, induced by the same cosmic ray muon, arrive at the same BX. Occasional difference by 1 BX is unavoidable due to the fact that cosmic rays are asynchronous to the clock of the experiment and because the relative synchronisation between different detector parts obtained with cosmic rays has a finite precision of several ns. The CSC timing was adjusted during CRAFT, to improve the synchronisation. The top half of CSC was delayed by 2 BX and the bottom half was delayed by 1 BX. The dashed line in figure 6 shows the situation before this adjustment, and the solid line shows the situation afterwards.

Similarly, delays of calorimeter trigger inputs to the Global Trigger have been adjusted to provide the highest coincidence rate above the noise continuum. In this way, the e/γ trigger and technical triggers from HCAL were adjusted. The timing of the jet trigger, which was in the early stage of commissioning during CRAFT, was adjusted shortly after the CRAFT exercise. Relative timing of calorimeter triggers with respect to DT muon triggers is shown in figure 7.

4.6 Synchronisation with LHC beam

During LHC operations, the BPTX technical triggers were enabled. Their timing with respect to muon and calorimeter triggers could be tested only in the presence of the beam. Initial synchronisation was achieved using the “beam splash” events. The beam producing these events was always injected at the same phase with respect to the orbit signal. Using the muon beam halo trigger provided by the CSC system and the HF technical trigger, which both have very low background from cosmic rays and noise (total rate less than 3 Hz), it was possible to see a clear signal in the BX distribution just after a few beam shots (figure 8). The BX distribution is produced by counting LHC clocks (40 MHz) and resetting the counter by a signal derived from the LHC orbit signal. The upstream CSC endcap was delayed by 2 BX to provide a trigger in coincidence with the downstream endcap. This information was then used to delay the BPTX trigger signal and align them with muon and calorimeter triggers. Satellite peaks in the HF are due to afterpulses in HF phototubes filtered through trigger rules. The procedure was repeated also with the circulating beams. Figure 9 shows

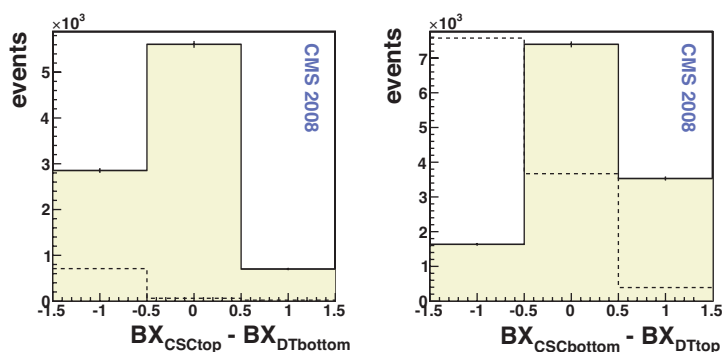


Figure 6. Time differences at the GMT in terms of BX between L1 muon candidates - created in most cases by the same cosmic ray muon - from top half of the CSC and bottom part of the DT system (*left*), and from bottom part of the CSC and top part of the DT system (*right*). The dashed line shows the situation before the modification to CSC timing (top delayed by 2 BX and bottom delayed by 1 BX) mentioned in the text.

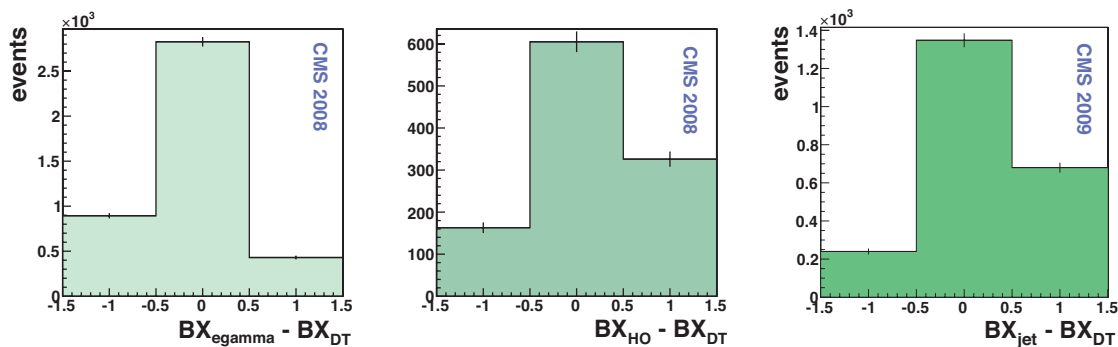


Figure 7. Time differences at the GT input between e/γ triggers (*left*), HO technical triggers (*middle*), and jet triggers (*right*, 2009 data), with respect to L1 muon candidates from the DT system.

the distribution of the CSC muon halo and BPTX triggers within the LHC orbit, as a function of time. The rate of both triggers increases during periods when LHC beam is circulating. As can be seen, the delay associated with the BPTX trigger was adjusted over the course of several LHC fills, and brought into synchronisation with the halo trigger.

5 Hardware validation using emulators

A full bit-level software emulation of the L1 trigger was developed alongside the hardware [22]. This serves two purposes: to simulate the trigger response in CMS simulation and to monitor the operation of the hardware. In the latter role, the input to a particular trigger subsystem is read out and used as input to a bit-level software emulation of that subsystem. The output of the emulator can be compared with the output of the subsystem for each event, to validate the trigger operation. In this section, the results of such comparisons performed with the CRAFT data are discussed.

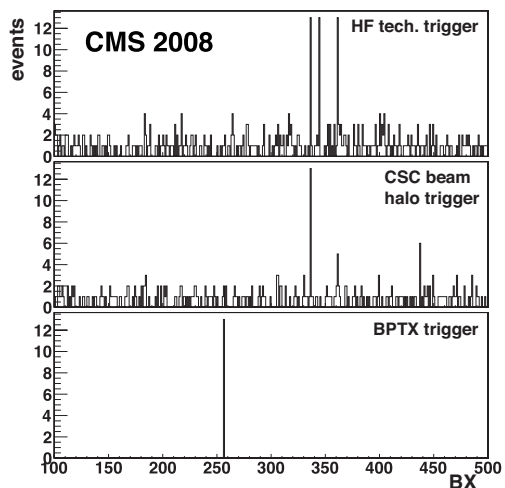


Figure 8. Measurement of the time delay in BX between the BPTX trigger and previously synchronised CSC beam halo and HF triggers, using beam splash events.

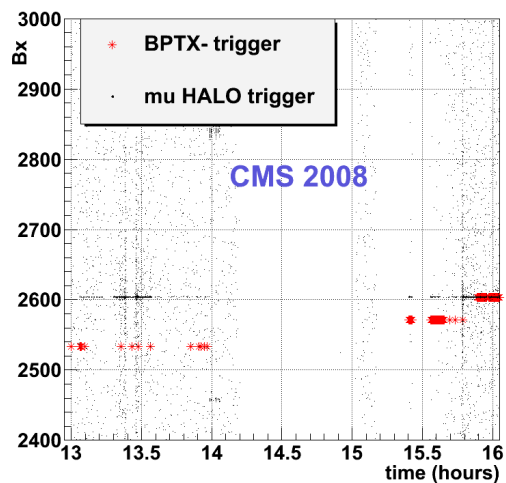


Figure 9. Synchronisation of the BPTX trigger with CSC beam halo trigger during circulating LHC beam.

These comparisons were run in offline analysis, and in automated online and offline data quality monitoring processes.

One general problem encountered when comparing emulator and hardware processing, is the need to ensure that the emulator is configured in the same way as the hardware. In future data-taking operations, automated database transfers synchronised with online run control will allow automatic configuration of the emulators running offline, and hence allow fully automated validation of every event stored. Unfortunately, during CRAFT, the database transfer system had not been fully commissioned, and subsystem configurations changed from run to run. Therefore, a subset of events has been used to validate each subsystem, rather than the entire CRAFT dataset. The results, presented below for each subsystem, show that the L1 trigger processing is in good agreement with the software emulation. Disagreements arise in some subsystems, at the few % level at most. Such disagreements generally indicate subtle differences between hardware and emulator algorithms, or hardware problems and have been followed up on since CRAFT.

5.1 Muon triggers

Validation of the DT trigger is complicated by the fact that the DT trigger primitives are digitised using a different technique and clock phase from that used for the full granularity readout. Precision time measurements are made using TDC data, whereas the trigger track segment time is calculated using a digital mean timer technique. Different clock phases are used to eliminate clock skew between trigger boards and achieve the best synchronisation for muons coming from LHC collisions. The difference in clock phase must be taken into account when emulating the trigger response from the full detector readout. For muons with LHC timing, the trigger primitives can be correctly emulated. For cosmic ray muons, which have a flat distribution in time, the emulator cannot be expected to reproduce muon times that are close to the trigger clock edge. Nevertheless, a data-emulator comparison was performed for 3×10^6 events, and 99% agreement was found in

the trigger efficiency as a function of track position and impact angle. This result is consistent with what can be expected from the emulator given the timing issue outlined above.

The remaining muon trigger subsystems, apart from CSCTF, were validated by emulating outputs from read out input data. The DTF validation was performed for 1 Million events in a run that used “closed LUTs” (the “open LUTs” used for cosmic ray data taking are not emulated) where the muon remains in a single DT sector. 100% agreement was observed between emulator and data. For a typical run, the emulated CSC trigger primitives agreed with those in the data in 99.5% of events. The remaining 0.5% were due to a minor firmware error that has since been corrected. The RPC trigger validation showed disagreement between data and emulator in $\sim 2\%$ of cases, again for a typical run, coming almost exclusively from muon candidates in particular detector regions. The GMT validation was performed regularly, with a typical run showing 100% agreement between data and emulator.

5.2 Calorimeter triggers

The calorimeter readout includes full granularity ECAL crystal and HCAL tower data, as well as the trigger primitives sent to RCT. The trigger readout includes e/γ candidates and region sums at the output of the RCT, and the e/γ and jet candidates at the output of GCT. Validation of the calorimeter trigger processing therefore involves emulation of:

- ECAL trigger primitives from full granularity crystal data;
- HCAL trigger primitives from full granularity HCAL towers;
- RCT e/γ candidates and region sums from ECAL trigger primitives in data;
- GCT e/γ and jet candidates from RCT e/γ candidates and region sums in data.

The ECAL validation was performed on 10 Million events, constituting the bulk of runs where ECAL crystal data was not zero-suppressed. After accounting for masked channels, agreement was observed between the emulated E_T and fine-grain bit and the data in more than 99.9% of trigger primitives.

The HCAL validation was performed on over 50 Million events. Both E_T sums and the HF fine-grain bit were compared between emulator and data. The level of disagreement observed between emulator and data was less than 1×10^{-6} .

The RCT validation takes ECAL and HCAL towers from ECAL/HCAL readout data and produces emulated e/γ candidates, which are then compared with those read out by the GCT. Disagreements at the level of a few percent were observed in 2008 due to masked channels that were not emulated and latency instability in the HCAL data. During cosmic ray data-taking in 2009, the comparison is performed on a regular basis and shows perfect agreement between data and emulator.

The GCT emulator validation was performed on 20 Million CRAFT events. Agreement was observed between hardware and emulator for 100% of e/γ candidates. A small error in the implementation of the jet-finding algorithm was discovered in the comparison of the jet candidates. In approximately 0.05% of cases a jet was incorrectly labeled as passing the τ -lepton veto. This has no impact on the efficiency and resolution studies presented later in this paper, and the firmware has since been corrected.

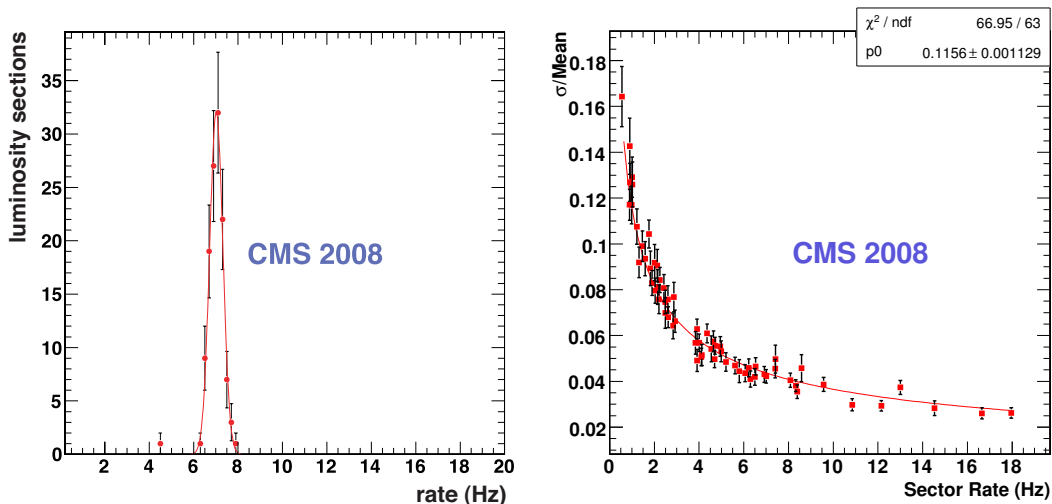


Figure 10. The rate distribution of a particular sector of wheel 0 (*left*). Fit to the $\sigma/mean$ of all measured sector rates (*right*).

6 Drift-tube trigger performance

Operating in “open LUTs” mode, the DTTF delivered about 240 Hz of muon candidates from the whole DT detector. The rate stability was tested by counting the number of DTTF tracks collected from each sector per “luminosity section”; a period of time lasting ~ 93 seconds. For each run, a sample of rate measurements was collected in a histogram, to which a single Gaussian function was fit. An example is shown in the left plot of figure 10 for sector 8 in wheel 0. The L1 trigger system could start to deliver L1 accepts several seconds after the data acquisition was started; thus the first luminosity section, which appears as an isolated point at the left of the Gaussian peak in the rate plot, has incomplete statistics and is not considered in the fit. The mean and sigma of the Gaussian were used to compute the $\sigma/mean$ for each active sector. In the absence of biases the $\sigma/mean$ is expected to scale with the square root of the number of events collected, consistent with a Poissonian distribution. To test this assumption another fit was performed on the distribution of the $\sigma/mean$ for each active sector with the function:

$$f(x) = \frac{p0}{\sqrt{(x)}}$$

The results of the fit are shown in the right plot of figure 10. The measured $p0$ is 10% higher than the naive expectation $1/\sqrt{L} \sim 0.103$, where L is the luminosity section length, due to trigger dead-time not taken into account in the rate calculation (see section 3.3) and other possible effects under investigation.

The coordinates assigned by the DTTF were compared to the coordinates obtained from the offline reconstruction of muon tracks using the muon detectors only (“standalone muons”). The comparison was performed for ϕ and η coordinates, but no p_T assignment study is possible with the CRAFT data (section 3). The L1 muon candidate position is reported at the extrapolated intersection of the track with a cylinder at the radius of the MB2 station. The offline track was therefore

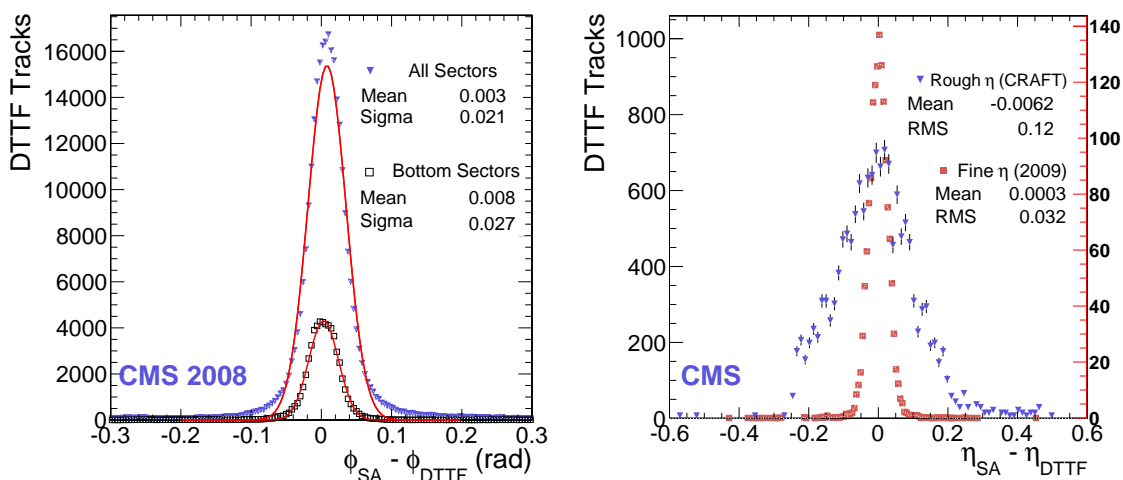


Figure 11. DTFF ϕ resolution (*left*). The ϕ difference between DTFF and offline standalone muons (SA) is shown. Both the distribution obtained from all sectors (*triangles*) and the one obtained from bottom sectors only (sectors 9,10 and 11, *squares*) are shown. DTFF η resolution (*right*). The η difference between DTFF and offline standalone muons (SA) is shown. The low-resolution η assignment, the only possibility during CRAFT 2008, is shown with blue triangles. For comparison, high-resolution η assignment is shown with red squares (from 2009 data).

propagated to the MB2 cylinder, and the position of the intersection point compared to the trigger data. Events with tracks in masked sectors or with known hardware problems were rejected in the analysis.

The difference between the coordinate from the reconstructed track and the DTFF ϕ value is shown in the left plot of figure 11. Only positive wheels were used, as the negative wheel coordinate assignments were not implemented properly. This was a consequence of misconfiguration of the hardware modules delivering trigger primitives, which was corrected and validated after CRAFT. Two histograms are shown, one including all sectors and one for bottom sectors only (sectors 9, 10 and 11). In the bottom sectors the muon direction, and hence multiple scattering and energy loss effects, are LHC-like, so the resolution improves to $\sigma \sim 0.021$ rad and the tails in the distribution are removed.

As mentioned in section 3, the DTFF η assignment was not yet commissioned in CRAFT, as trigger primitive θ -view information was not yet delivered to the track finder. Nevertheless, a subset of the system could assign low-resolution η values using the ϕ -view primitives. The right plot of figure 11 shows the difference of trigger and offline η values assigned during CRAFT. For comparison, the same quantity is shown for cosmic ray data taken in 2009, at a time when fine-resolution η assignment based on trigger primitive θ hits was possible. The η assignment between the DTFF and the reconstructed muons is in good agreement.

The DT trigger efficiency was evaluated using offline standalone reconstructed muon tracks, that were required to intersect the CMS tracker volume. Only tracks traveling from the top to the bottom of the detector were kept, as low p_T muons can bend back and exit the detector from the top side. A minimum track momentum of 5 GeV/c was required, and only tracks with at least 20 hits

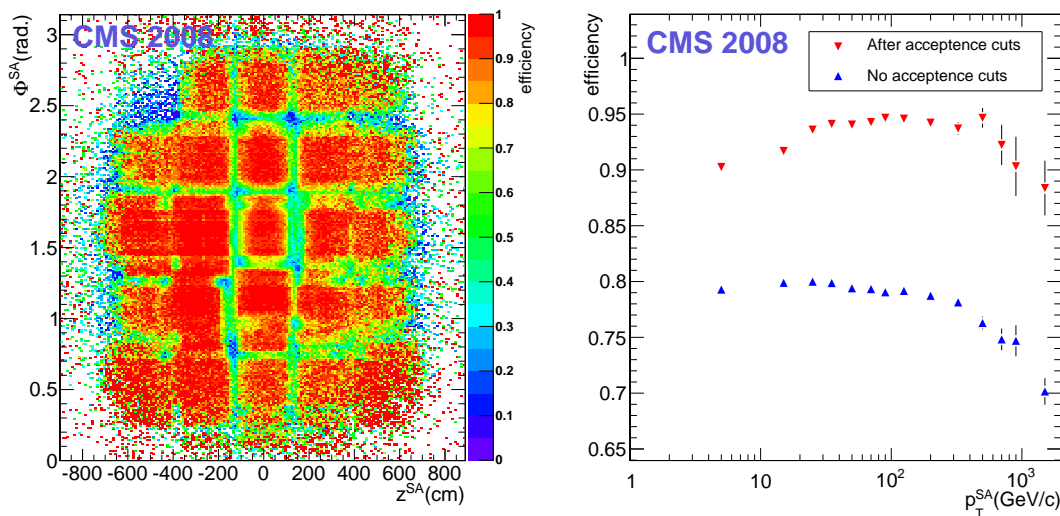


Figure 12. Left: DT trigger efficiency for the upper half of the detector as a function of (ϕ, z) of the standalone track (SA), computed at the position of the MB2 station. Right: DT trigger efficiency as a function of the p_T of the standalone track; the two data series correspond to efficiencies computed with and without acceptance cuts (see text).

in total from DT and RPC detectors were kept, as this ensures the presence of local track segments in at least two stations resulting in acceptable p_T resolution.

Tracks reconstructed in the bottom half of the detector, with a matching trigger candidate, were used to probe the efficiency of the top half of the detector in an unbiased way. This was done by propagating the track to the second muon station in the top and looking for a matching trigger candidate. If a DTTF track was found, the trigger was considered efficient in this event.

In figure 12, left, a (ϕ, z) map of the efficiency computed in this way is shown. Besides the very low occupancy around $\phi \sim 0$ and $\phi \sim \pi$, due to the low rate of horizontal cosmic rays, the main features visible are a lower efficiency in cracks between detector sectors, and a whole sector missing (wheel -2, sector 6, closest to $\phi = \pi$). This was due to a malfunctioning hardware module that had been masked.

To check the intrinsic performance of the DT trigger system, tracks passing through the central portion of the top 3 sectors only were considered. Tracks passing within 5° in ϕ , or 50 cm in z , of a sector boundary were ignored. The results are summarized in figure 12 (right), where the efficiency versus the p_T of the muon track is shown, before and after the removal of the crack regions. The efficiency after the removal of the cracks reaches about 95%, while it drops to about 80% without the acceptance cut. The acceptance losses between wheels are due to the loose pointing requirements used to select the muons which allow a significant fraction of vertical muons.

7 Cathode strip chamber trigger performance

The total output trigger rate from the CSCTF was ~ 60 Hz. The distributions of trigger rates in each 60° CSC trigger sector are shown in figure 13. The trigger rate ranges from 4.5 Hz to

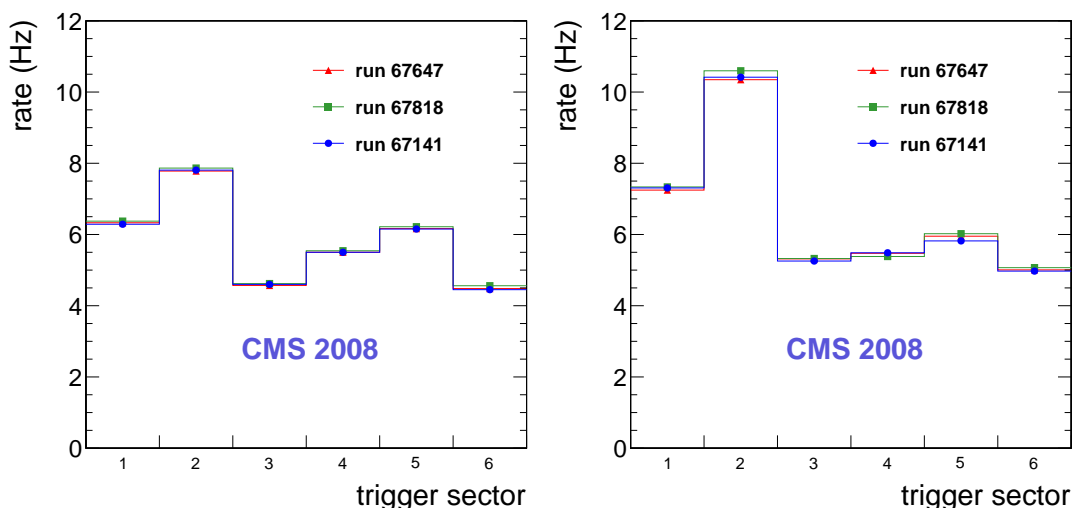


Figure 13. CSC trigger rates by sector during CRAFT. Several typical long runs were selected to calculate the trigger rates. Rates from these runs show good agreement. The left plot shows the trigger rate from the $z > 0$ endcap; the right plot is for the $z < 0$ endcap.

10.5 Hz for different trigger sectors according to their different positions. Several features of the trigger rate distributions are visible: the differences of top (1-3) and bottom (4-6) sectors and the other ϕ dependencies reflect the spatial distribution of cosmic rays penetrating CSC chambers, as well as the angular acceptance of strip and wire trigger primitive pattern templates. There are also asymmetries between endcaps, which are caused by the higher muon rate at the negative side of the detector, which is below the CMS main access shaft.

The assignment of ϕ , η , and p_T by the CSCTF has been compared with that of offline reconstructed muons. While the aim of the CSCTF is to identify collision muons, cosmic ray muons may arrive from all possible directions. For this reason, these studies use only muons whose direction points to the interaction point, to resemble the expected behavior of collision muons. In addition, all candidates tagged by the CSCTF as halo muons were removed, along with those where only one segment was found in the CSCTF, since the ϕ assignment of such candidates was not properly implemented at the time of CRAFT.

The ϕ angle assignment is shown in figure 14. These plots show the comparison between the ϕ measured by the CSCTF, with respect to that measured by the offline muon reconstruction, and the ϕ resolution with an overlaid Gaussian fit, respectively. The ϕ assignment between the CSCTF and the reconstructed muons is in good agreement. In fact most of the candidates lie on the diagonal line, as shown in the left plot in figure 14.

The p_T analysis requires a tighter muon selection. The CSCTF assumes that muon tracks originate from the interaction point, and the p_T assignment takes into account loss of momentum as they traverse the detector. Therefore, only muons following a similar trajectory, traversing the interaction region before crossing the bottom half of the detector, are included in the analysis. The muon, reconstructed offline, is required to have at least one hit in the CSC detector, and at least 10 hits in the central tracker, to benefit from the best p_T resolution for the reconstructed candidates. Figure 15 shows the mean p_T assigned by CSCTF (p_T^{CSCTF}) as a function of the p_T

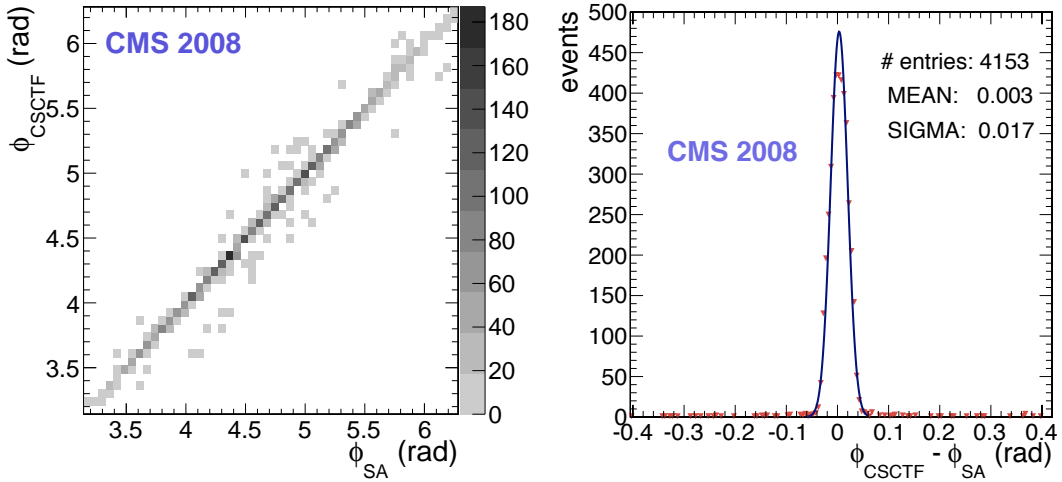


Figure 14. CSCTF ϕ resolution. Left: comparison between the ϕ measured by the CSCTF (“ ϕ_{CSCTF} ”) and the ϕ estimated from the offline standalone reconstruction (“ ϕ_{SA} ”). Right: distribution of the ϕ resolution with an overlaid Gaussian fit.

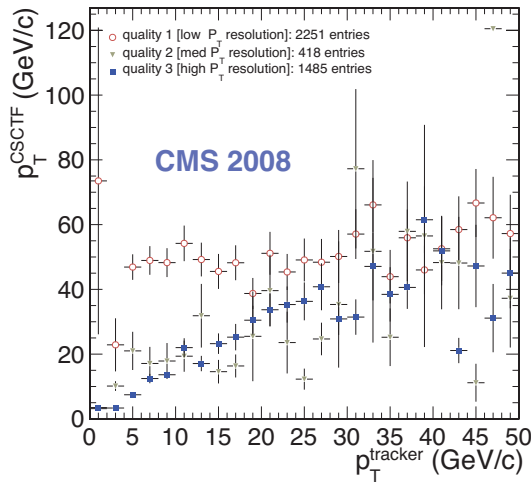


Figure 15. Mean p_T assigned by the CSCTF as a function of the p_T measured by the offline reconstruction, separated in bins of CSCTF p_T resolution corresponding to a quality tag assigned by the CSCTF algorithms.

measured by the tracker system ($p_T^{tracker}$). For a precise understanding of the performance, the comparison is broken in bins of quality of CSCTF p_T resolution. Several conclusions can be drawn. Since quality 3 corresponds to high p_T resolution CSCTF tracks, the distribution flattens at higher p_T reconstructed value, compared with the quality 2 p_T distribution (medium p_T resolution). As expected, the CSCTF p_T assignment for quality 1 tracks is not well correlated with the tracker p_T measurement. It should be noted that quality 1 tracks are only used in LHC collision trigger menus as the second leg of a di-muon trigger, with essentially no p_T requirement.

The efficiency of CSC muon identification was studied, for both the single track segment mode

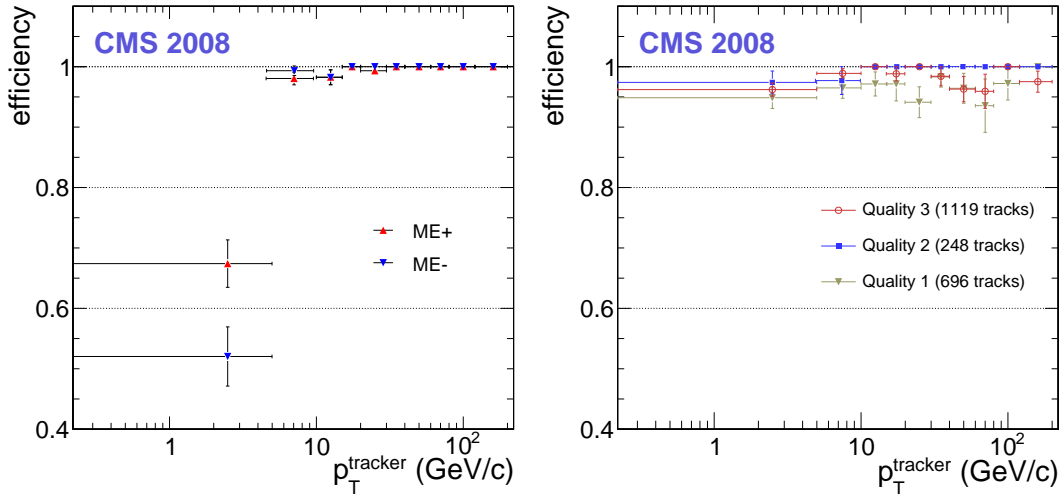


Figure 16. Left: efficiency of CSCTF in “singles” mode as a function of offline reconstructed p_T in the tracker, p_T^{tracker} , for each endcap separately. Right: efficiency of CSCTF to build a muon candidate from several track segments separated in bins of a quality tag assigned by the CSCTF algorithms.

and the track-coincidence mode. For the “singles” mode, the efficiency of one endcap is measured using events taken with a trigger in the opposite endcap earlier in time. An offline reconstructed muon is required, pointing towards the IP, with p_T above 10 GeV/c. The central tracker track is extrapolated into the CSC endcap under study, and a CSCTF candidate is searched for within $\delta\phi < 0.3$ radians. Figure 16 shows that the efficiency is greater than 99% for both endcaps on $\sim 2k$ events with IP pointing tracks of p_T above 20 GeV/c.

In the track-segment matching mode of operation, the CSCTF builds tracks as a coincidence of 2, 3, or 4 track segments from different stations. The CSCTF logic suppresses candidates from the “singles” mode if it can form a coincidence from the received segments. The efficiency of the track coincidence mode, relative to the singles mode, was measured by considering all CSCTF candidates (singles and coincidence), and checking for other available segments in the other stations in the same time bin. If segments which could form a coincidence were found, a corresponding multi-segment CSCTF candidate was searched for. The resulting efficiency, broken in bins of quality, is shown in the right plot of figure 16. The relatively large fraction of quality 1 candidates is due to the loose geometric requirements used for cosmic ray muons.

8 Resistive plate chamber trigger performance

The average rate of the muon candidates produced by the RPC trigger was about 140 Hz. However, periodic disturbances visible as spikes in the trigger rate were observed and were the subject of detailed studies on both the RPC chamber and the trigger electronics. Dedicated data were taken for the RPC noise studies. Although never observed before CRAFT, periodic noise effects were found to be correlated with electric disturbances coming from external sources and related to underground daytime activities in UXC, rather than connected with the CMS magnetic field itself. They were found to be sensitive to the discriminator thresholds and completely absent in the trigger path if no

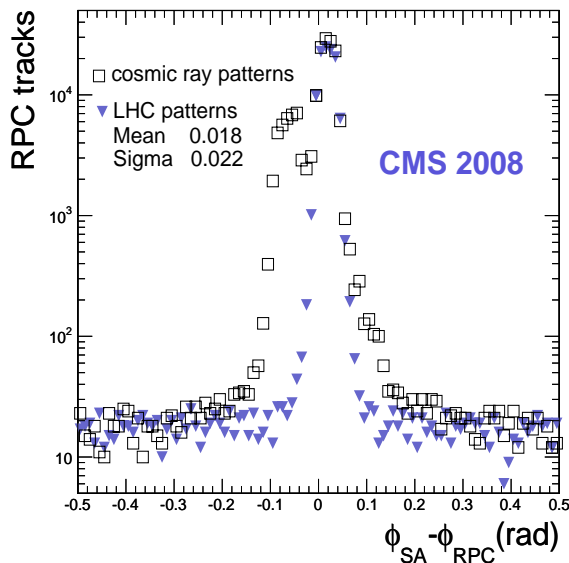


Figure 17. Resolution of the RPC trigger: RPC trigger ϕ minus reconstructed muon ϕ for cosmic ray patterns used in CRAFT data taking (dashed line), and for beam collision patterns, produced by running the RPC trigger emulator over the same data sample (solid line).

signal from the chambers was delivered. The noise was found to be mostly coherent and it can only be partially eliminated by changing the trigger logic to require more planes in coincidence. The standard configuration for cosmic rays, implemented with the requirement of a coincidence in 3 out of 6 chamber planes, was compared to a modified coincidence requirement of 4 out of 6 chamber planes obtained in offline emulation of the trigger. The modified trigger logic is found to reduce the noise peak values from up to 1100 Hz to up to 220 Hz, but it also decreases the overall average trigger rate, which drops from about 140 Hz to 45 Hz. It should be stressed that when the RPC readout data were processed by the RPC trigger emulator using LHC patterns, the rate spikes were completely eliminated. This is due to a combination of using a coincidence of 4 out of 6 planes with the fact that LHC patterns are much narrower. During and since CRAFT, steps were taken to identify the sources of noise. Since the summer of 2009, the noise has been reduced to a marginal problem.

The ϕ resolution of the RPC trigger was studied by comparing the ϕ values from the RPC track finder with those from standalone muons reconstructed using DT segments. A typical result is shown in the open histogram of figure 17. A two-peak structure can be seen, which is an artefact of the ghost removal algorithm in the case of cosmic ray patterns. Since a p_T measurement was not made by the RPC trigger in CRAFT, the ghost removal algorithm saves only the muon candidate with higher ϕ value whenever two muon candidates in a given sector are found from overlapping logical cones. Such events produce a systematic bias in the ϕ measurement, visible as an additional peak shifted by 6 degrees on average. To confirm this, the resolution was obtained using patterns for LHC collisions, as shown in the solid histogram of figure 17. The additional peak is not present in this case.

The RPC trigger efficiency is evaluated using standalone reconstructed muon tracks, with method and selections as detailed for the DT trigger in section 6. These data were taken at a

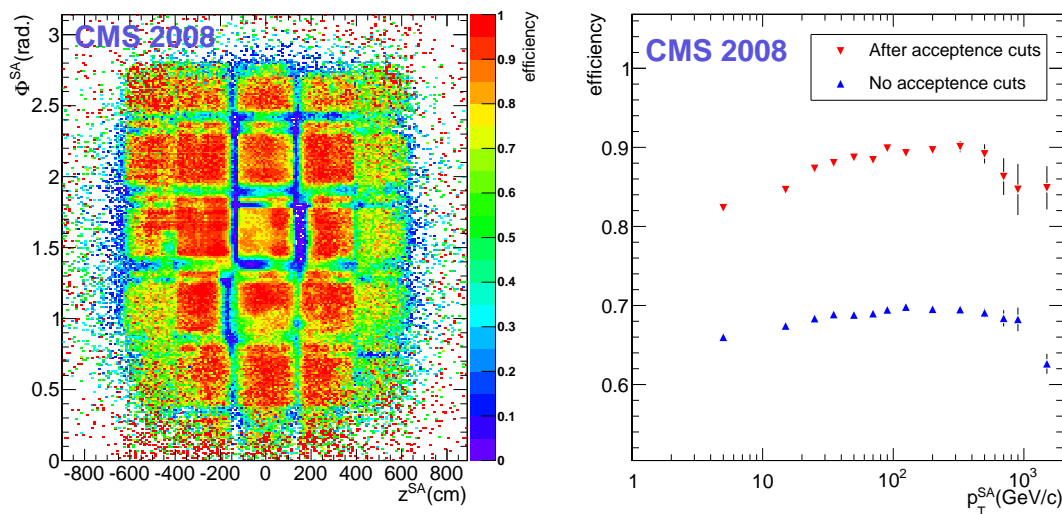


Figure 18. RPC trigger efficiency as a function of (ϕ, z) of the standalone reconstructed muon, computed at the position of the MB2 station (*left*). RPC trigger efficiency as a function of the p_T of the standalone muon. The two data series correspond to efficiency computed with and without acceptance cuts (see text).

chamber voltage of 9.2 kV. Figure 18 (left) shows a (ϕ, z) map of the efficiency computed in this way. The main visible features are a lower efficiency in cracks between detector sectors and very few events near $\phi = 0$ and $\phi = \pi$ due to lack of horizontal cosmic rays. In figure 18 (right), the efficiency versus the p_T of the muon track is shown, before and after the removal of the crack regions. The efficiency after the removal of the cracks is between 85 and 90% in the central p_T region, with a clear tendency to increase with p_T , while it drops to about 70% without the acceptance cut. Work to understand the efficiency result is ongoing. The systematic biases due to the method are expected to play some role and are presently under evaluation.

9 Electron/photon trigger performance

The performance of the barrel e/γ trigger has been evaluated in terms of rate, resolution and efficiency. The distribution of the rate of the L1_SingleEG1 e/γ trigger, which nominally fires whenever a single electromagnetic energy deposit above 1 GeV is detected, is shown in figure 19 for a typical CRAFT run. The L1 decision is based on the sum of 2 towers of 25 ECAL crystals each. The average single crystal noise as measured during the entire running period was 40 MeV [23], so the L1 candidate noise is expected to be around 280 MeV. On the other hand, a rate of 22.65 Hz implies that the threshold of the L1_SingleEG1 trigger is roughly 5σ away from the detector noise. As will be seen later in this section, the L1_SingleEG1 trigger turn-on point corresponding to 50% efficiency is measured to be 1.19 GeV, implying the noise of the particular run in figure 19 is around 240 MeV. Given that the expectation is derived from a much larger period of time, the agreement is found to be good.

To study the trigger resolution and efficiency, ECAL superclusters (SC) originated by muon radiation in the lead tungstate crystals and reconstructed offline as described in [23] are used as tags to probe for the production of L1 e/γ trigger candidates.

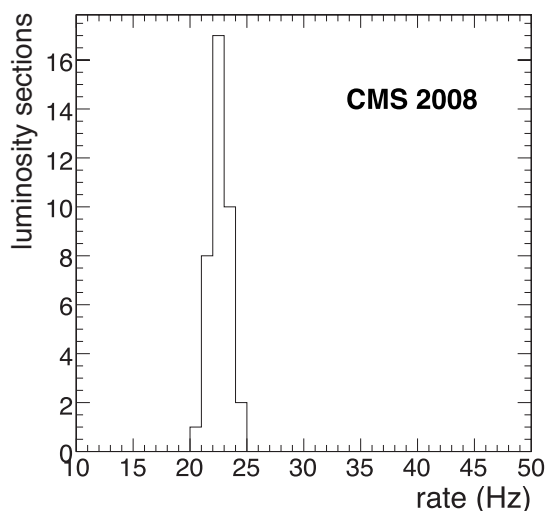


Figure 19. Rate distribution of the L1.SingleEG1 trigger for a typical run. The average rate is compatible with that expected from the noise level measured in the ECAL.

9.1 Data selection

The e/γ trigger resolution and efficiency were measured using events taken with a muon trigger. Online data reduction for the ECAL was obtained through the selective readout algorithm [24], which classifies the detector into regions of low or high interest. Low interest regions were read out using zero-suppression on a crystal-by-crystal basis, whereas in high interest regions full readout is done, preserving the information of all crystals involved in the trigger decision. For the full trigger chain efficiency measurement a complete configuration of the full L1 e/γ trigger is required: namely the ECAL, the RCT and the GCT. For the trigger primitive generator efficiency measurement, only the ECAL trigger primitive generator need be configured. Finally, the study used only the regions of the detector that had no known hardware problems.

In selecting ECAL superclusters, at least one crystal with a reconstructed energy above 400 MeV is required, ten times the noise RMS. This ensures accurate timing reconstruction [25] and by retaining events within 3.75 ns of the trigger, rejects asynchronous cosmic ray deposits. In contrast to the cosmic ray signal reconstruction that fits an asynchronous pulse shape to the 25 ns signal samples, here the signal amplitude, and consequently E_T , are reconstructed using a weighted sum of the signal samples. Not only is this the standard procedure for beam collision data, it is also better suited for comparison with trigger quantities, since the trigger amplitudes determined in the detector front-ends are obtained using a similar weighted sum method.

Finally, the ECAL superclusters are required to be validated by an offline-reconstructed global muon. Validation is based on the distance, ΔR , between the ECAL supercluster position and the linear extrapolation of the muon track to the ECAL inner surface [26] (μ), starting from the tracker. Events are retained with $\Delta R(\text{SC}, \mu) < 0.1$.

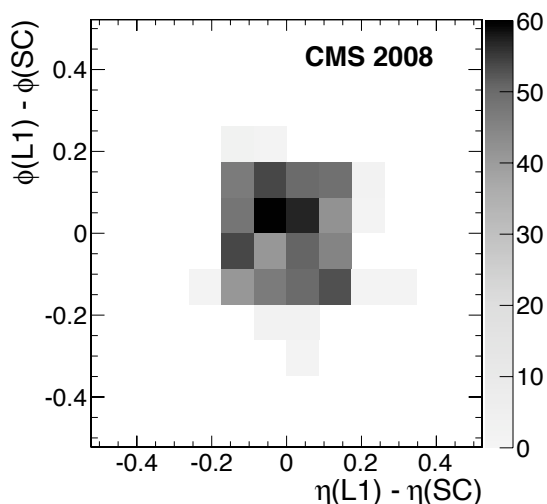


Figure 20. $\Delta\eta$ and $\Delta\phi$ of Level-1 e/γ trigger objects with respect to reconstructed ECAL superclusters.

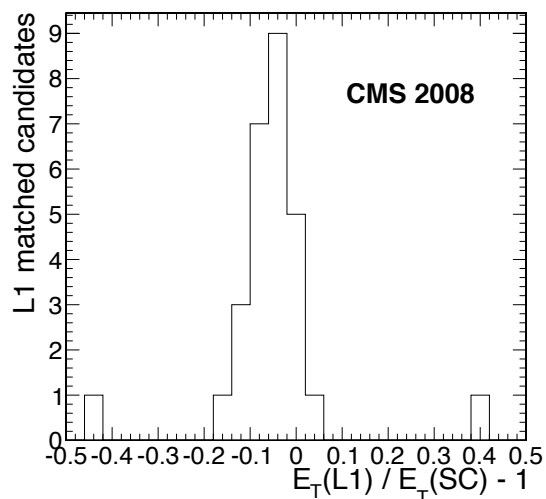


Figure 21. Level-1 e/γ E_T resolution for $E_T(L1) > 10$ GeV. The non-zero mean results from a combination of factors and is compatible with the LSB of $E_T(L1)$.

9.2 Resolution and efficiency

After obtaining a pool of ECAL superclusters validated by reconstructed muons, the L1 e/γ trigger resolution and efficiency were probed. The distributions for $\Delta\eta = \eta(L1) - \eta(SC)$ and $\Delta\phi = \phi(L1) - \phi(SC)$ are shown in figure 20 for L1 candidates satisfying the L1_SingleEG1 requirement of $E_T(L1) > 1$ GeV. The binning used corresponds to the dimensions of one ECAL trigger tower, 0.087 in both η and ϕ . The highly populated region of 4×4 ECAL trigger towers corresponds to the resolution with which the L1 e/γ candidate position is reported.

Figure 21 shows the relative difference between $E_T(L1)$ and $E_T(SC)$ for $E_T(L1) > 10$ GeV. The resolution from fitting a Gaussian to the distribution is 5.2% and the mean -4.7% . The non-zero mean is caused by differences in the way E_T is calculated in L1 and off-line reconstructions. These are: the clustering algorithm, the signal amplitude determination, and the effect of integer truncation in the L1 E_T determination, which has a LSB of 500 MeV. Each of these effects contributes to the L1 E_T being lower than the E_T which is recovered offline, the effect above 5 GeV being of the order of the LSB. The resolution is also of the order of the LSB; due to the steeply falling energy spectrum of these events, the sample is dominated by those just above the 10 GeV threshold.

To further characterize the e/γ trigger, two efficiencies were measured: the trigger primitive (TP) generator efficiency and the Level-1 e/γ candidate efficiency, which correspond to the first and the last steps in the calorimeter trigger chain. Due to the requirement of an energy deposit in the ECAL, this measurement evaluates the trigger efficiency only in the active part of the detector and is relative to the detector efficiency to detect muons and electromagnetic energy.

The trigger primitive generator is considered efficient if a muon-tagged ECAL supercluster has an associated TP in the same ECAL trigger tower. The TPG efficiency is shown in figure 22 (left) as a function of $E_T(SC)$. It rises with increasing $E_T(SC)$ before reaching a plateau of 100%,

the 50% efficiency turn-on point being at 0.70 ± 0.03 (stat.) ± 0.02 (syst.) GeV, compatible with the threshold set at 750 MeV (section 3). The systematic error is determined by varying the cuts applied to the selection.

The full e/γ trigger chain is considered efficient if a muon-tagged ECAL supercluster has an associated L1 e/γ candidate with energy above the L1 e/γ threshold under study. The measure of association used is the distance between the L1 candidates and muon-tagged ECAL superclusters, $\Delta R(L1, SC^\mu)$. Despite the coarse (η, ϕ) resolution of L1 e/γ candidates (figure 20) two classes of events can be clearly distinguished: events where the L1 e/γ candidate matches the muon-tagged ECAL supercluster around $\Delta R = 0$ and events where the objects are in opposite sides of the experiment with $\Delta R > 3$. The latter case is expected since some muons cross the ECAL leaving 2 energy deposits, one on the top and one on the bottom.

If $\Delta R(L1, SC^\mu) < 0.5$ and the L1 e/γ candidate rank is above the threshold under study, the event is considered efficient. With this selection the efficiency for the L1 e/γ trigger chain is shown in figure 22 (right) for three different trigger algorithms: L1_SingleEG1, L1_SingleEG5 and L1_SingleEG10 with nominal thresholds at 1, 5 and 10 GeV, respectively. An unbinned maximum likelihood fit of an error-function was performed for each of the datasets.

The turn-on point of the 1 GeV threshold algorithm, L1_SingleEG1, is found to be 1.19 ± 0.02 (stat.) ± 0.02 (syst.) GeV. For the corresponding 5 and 10 GeV algorithms the turn-on points are measured to be 5.23 ± 0.09 (stat.) ± 0.14 (syst.) GeV and 10.2 ± 0.2 (stat.) ± 0.3 (syst.) GeV, respectively. Systematic errors were estimated by varying the timing selection window from ± 1.25 ns to ± 5 ns and the tagging distance $\Delta R(SC, \mu)$ from 0.1 to 0.5. The discrepancies between the measured and expected turn-on points are a reflection of the effects already mentioned above, and mainly affect the L1_SingleEG1, since the L1 e/γ E_T LSB is 500 MeV. Above 10 GeV the effect is of no appreciable consequence.

10 Jet trigger performance

Towards the end of the CRAFT data taking, a jet trigger was enabled and was active in around 20% of the total runs. Due to the commissioning nature of the jet data taken, results based on only a few well-understood runs are presented. Figure 23 shows the measured rate per luminosity section in a single run for the single jet trigger with an E_T threshold of 10 GeV. The rate is dominated by detector noise, but is stable over the course of the run.

The Level-1 jet E_T assignment was compared with that of offline reconstructed jets, which were found using an iterative cone algorithm with a cone size of $\Delta R = 0.5$ [27]. The Level-1 jets were matched to the closest offline jet within a cone of $\Delta R = 0.5$. The resulting E_T resolution, defined as $E_T(L1)/E_T(jet) - 1$ (where $E_T(L1)$ and $E_T(jet)$ are the E_T of the matched L1 and offline jet, respectively), is shown in figure 24. The RMS is 0.16 and shows that the L1 jet E_T is around 70% of the offline jet E_T .

The efficiency of the jet trigger, relative to offline reconstructed jets, was measured with a data sample triggered using the electron trigger path. The electron trigger hardware is independent of the jet trigger. An iterative cone jet-finder algorithm with a cone size of $\Delta R = 0.5$ was run on the offline calorimeter data, and jets satisfying $|\eta| < 3.0$ and $E_T > 5$ GeV were selected. The jet trigger efficiency was measured relative to the selected jets by demanding a L1 jet, firing the trigger, within

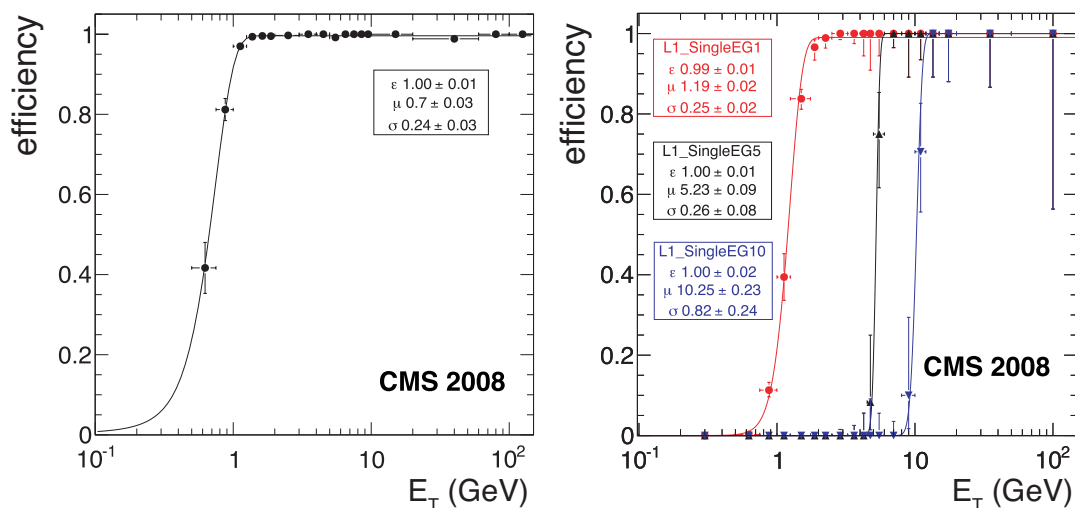


Figure 22. The ECAL trigger primitive production efficiency (left) and the full Level-1 e/γ trigger efficiency (right) as a function of the E_T reconstructed offline in ECAL. Parameters are obtained from fits of error functions to the data. In the case of the right figure, an unbinned fit was used.

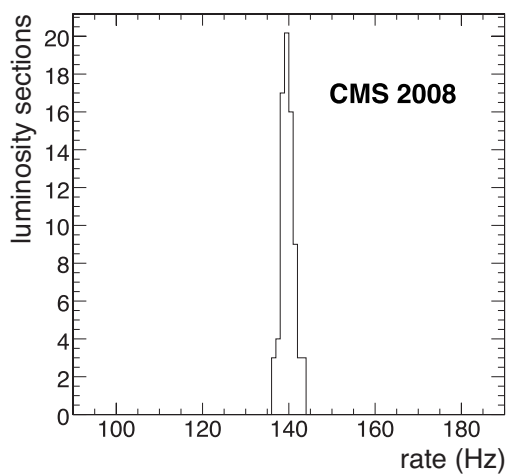


Figure 23. The distribution of the rate of the single jet trigger with an E_T threshold of 10 GeV.

a $\Delta R = 0.5$ cone of the offline jet. A data sample containing around 5000 offline jets was used to determine the efficiency of the single jet $E_T > 10$ GeV trigger as a function of the E_T , η , and ϕ of the offline jets, shown in figure 25. The results show that the jet trigger efficiency reaches the level of 90% at 20 GeV, and 100% at 40 GeV. The efficiencies in η and ϕ measured for jets with $E_T > 25$ GeV are uniform as expected.

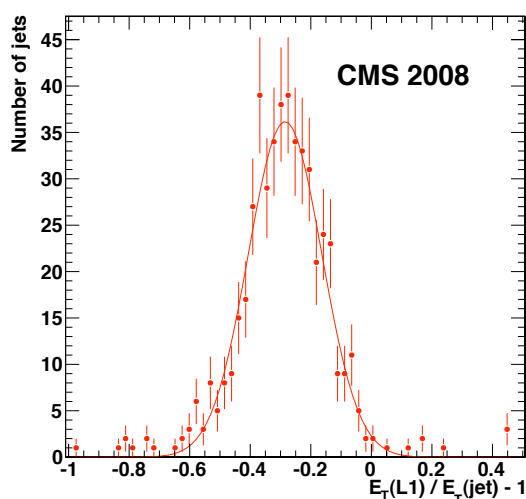


Figure 24. The E_T resolution of L1 jets.

11 Summary and outlook

The Level-1 trigger was operated stably during the period of LHC single beam operation, and later during the CRAFT cosmic ray data-taking period. All muon sub-detector triggers have been synchronised and shown to provide good trigger efficiency. The CSC muon candidate η , ϕ , and p_T assignments have been shown to work well, along with DT and RPC assignments. The e/γ trigger has been shown to be fully efficient. The jet trigger was commissioned during CRAFT and shown to be efficient across the detector. Together, these triggers have provided high quality cosmic ray event samples, as well as instrumental noise events necessary for understanding the detectors. The LHC beam monitoring technical triggers and the CSC beam halo trigger were operated and synchronised during LHC single-beam operations.

Since the CRAFT data-taking in 2008, CMS has taken weekly cosmic ray runs, which have allowed a development and testing of additional functionality. Optical links to the DT Track Finder for the θ view trigger primitives have been installed, improving the η assignment. Long runs have been taken with “LHC-like” look up tables in the DT track finder, allowing the p_T assignment to be validated. The links that share trigger primitives between DT and CSC systems in the barrel-endcap overlap region have been commissioned, and the DT trigger primitives have been synchronised at the CSC track finder. The RPC and ECAL endcap triggers have been commissioned. The remaining calorimeter energy sum triggers have been commissioned. A six week long cosmic ray run in the summer of 2009 allowed a large cosmic ray and detector noise dataset to be acquired using the new functionality. At the time of writing, analysis of this data is ongoing. The Level-1 trigger system is expected to stably and efficiently trigger on LHC collisions for CMS in the forthcoming run.

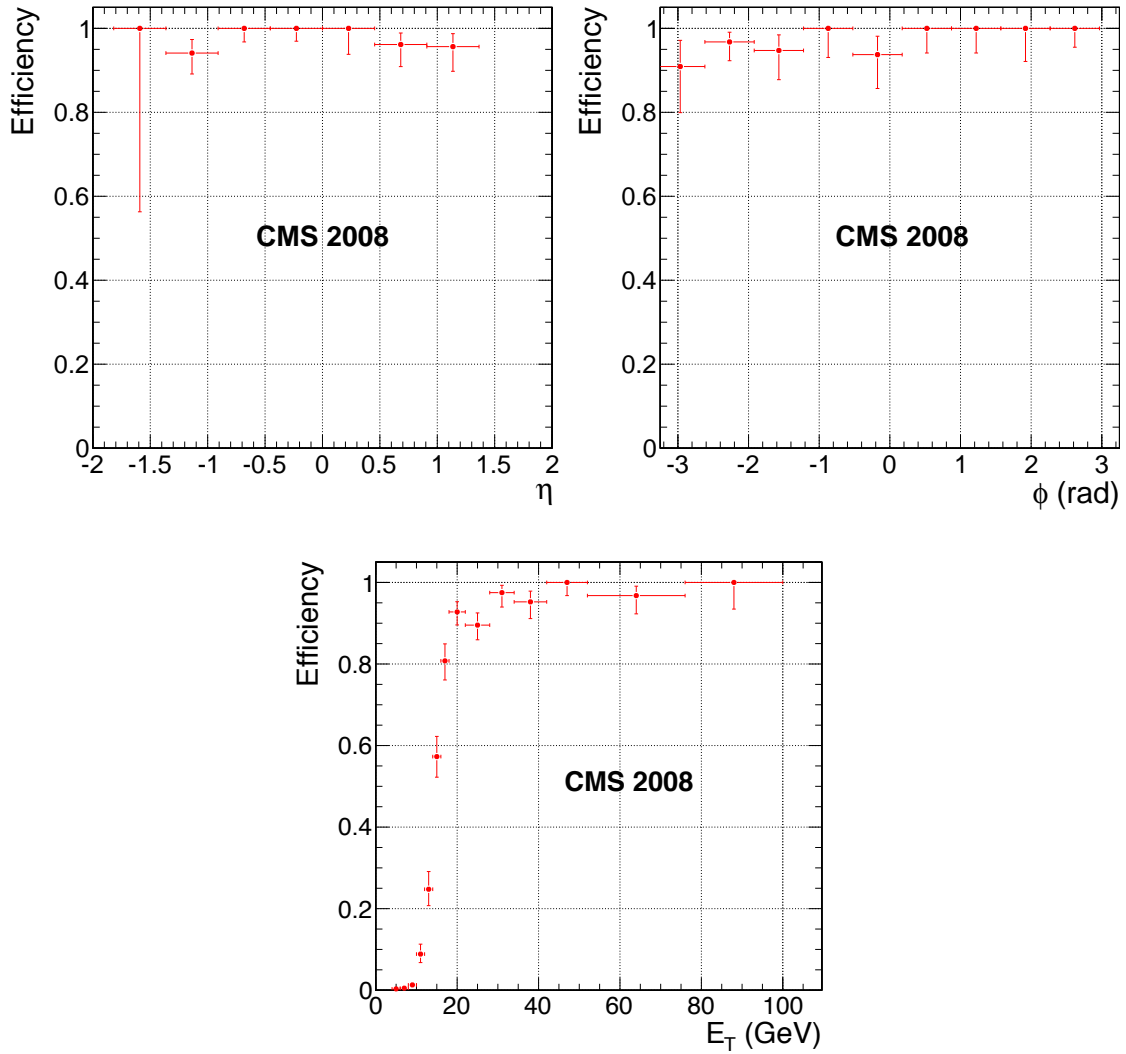


Figure 25. The efficiency of the single jet trigger with a L1 E_T threshold of 10 GeV, as a function of offline jet η , ϕ , and E_T (with $E_T > 25$ GeV for the η and ϕ plots).

Acknowledgments

We thank the technical and administrative staff at CERN and other CMS Institutes, and acknowledge support from: FMSR (Austria); FNRS and FWO (Belgium); CNPq, CAPES, FAPERJ, and FAPESP (Brazil); MES (Bulgaria); CERN; CAS, MoST, and NSFC (China); COLCIENCIAS (Colombia); MSES (Croatia); RPF (Cyprus); Academy of Sciences and NICPB (Estonia); Academy of Finland, ME, and HIP (Finland); CEA and CNRS/IN2P3 (France); BMBF, DFG, and HGF (Germany); GSRT (Greece); OTKA and NKTH (Hungary); DAE and DST (India); IPM (Iran); SFI (Ireland); INFN (Italy); NRF (Korea); LAS (Lithuania); CINVESTAV, CONACYT, SEP, and UASLP-FAI (Mexico); PAEC (Pakistan); SCSR (Poland); FCT (Portugal); JINR (Armenia, Belarus, Georgia, Ukraine, Uzbekistan); MST and MAE (Russia); MSTDS (Serbia); MICINN

and CPAN (Spain); Swiss Funding Agencies (Switzerland); NSC (Taipei); TUBITAK and TAEK (Turkey); STFC (United Kingdom); DOE and NSF (USA). Individuals have received support from the Marie-Curie IEF program (European Union); the Leventis Foundation; the A. P. Sloan Foundation; and the Alexander von Humboldt Foundation.

References

- [1] CMS collaboration, *The CMS experiment at the CERN LHC*, 2008 *JINST* **3** S08004.
- [2] L. Evans and P. Bryant eds., *LHC Machine*, 2008 *JINST* **3** S08001.
- [3] CMS collaboration, *Commissioning of the CMS experiment and the cosmic run at four tesla*, 2010 *JINST* **5** T03001.
- [4] CMS collaboration, *The TriDAS Project Technical Design Report: The Level-1 Trigger*, CERN-LHCC-2000-038 (2000).
- [5] H. Sakulin and A. Taurok, *Implementation and test of the first-level Global Muon Trigger of the CMS experiment*, in *Proceedings of the 11th Workshop on Electronics for LHC and Future Experiments* (2005).
- [6] L. Guiducci et al., *DT Sector Collector electronics design and construction*, in *Proceedings of the Topical Workshop on Electronics for Particle Physics* (2007).
- [7] J. Ero et al., *The CMS drift tube trigger track finder*, 2008 *JINST* **3** P08006.
- [8] D. Acosta et al., *A 3-D track-finding processor for the CMS level-1 muon trigger*, in *Proceedings of the Conference for Computing in High-Energy and Nuclear Physics* (2003).
- [9] CMS collaboration, *Alignment of the CMS muon system with cosmic-ray and beam-halo muons*, 2010 *JINST* **5** T03020.
- [10] RD5 collaboration, *Pattern Comparator Trigger (PACT) for the muon system of the CMS experiment*, *Nucl. Instrum. Meth. A* **370** (1996) 389.
- [11] M. Stettler et al., *The CMS Global Calorimeter Trigger hardware design*, in *Proceedings of the 12th Workshop on Electronics for LHC and Future Experiments* (2006).
- [12] G. Iles et al., *Revised CMS global calorimeter trigger functionality and algorithms*, in *Proceedings of the 12th Workshop on Electronics for LHC and Future Experiments* (2006).
- [13] M. Jeitler et al., *The level-1 global trigger for the CMS experiment at LHC*, in *Proceedings of the 12th Workshop on Electronics for LHC and Future Experiments* (2006).
- [14] I. Magrans de Abril, C.E. Wulz and J. Varela, *Concept of the CMS trigger supervisor*, *IEEE Trans. Nucl. Sci.* **53** (2006) 474.
- [15] J. Gutleber, S. Murray and L. Orsini, *Towards a homogeneous architecture for high-energy physics data acquisition systems*, *Comput. Phys. Commun.* **153** (2003) 155.
- [16] CMS collaboration, *Performance of the CMS drift-tube chamber local trigger with cosmic rays*, 2010 *JINST* **5** T03003.
- [17] CMS collaboration, *Link System and Crate Layout of the RPC Pattern Comparator Trigger for the CMS Detector*, CMS-NOTE-2002-022 (2002).
- [18] CMS collaboration, *Performance of the CMS drift tube chambers with cosmic rays*, 2010 *JINST* **5** T03015.

- [19] M. Aldaya et al., *Fine synchronization of the muon drift tubes local trigger*, *Nucl. Instrum. Meth. A* **564** (2006) 169.
- [20] CMS collaboration, *Fine synchronization of the CMS muon drift-tube local trigger using cosmic rays*, *2010 JINST* **5** T03004.
- [21] CMS collaboration, *Performance study of the CMS barrel resistive plate chambers with cosmic rays*, *2010 JINST* **5** T03017.
- [22] CMS collaboration, *CMS Level-1 Trigger Emulator*, in *Proceedings of the International Conference on Computing in High Energy and Nuclear Physics* (2009).
- [23] CMS collaboration, *Performance and operation of the CMS electromagnetic calorimeter*, *2010 JINST* **5** T03010.
- [24] N. Almeida et al., *Data filtering in the readout of the CMS electromagnetic calorimeter*, *2008 JINST* **3** P02011.
- [25] CMS collaboration, *Time reconstruction and performance of the CMS electromagnetic calorimeter*, *2010 JINST* **5** T03011.
- [26] CMS collaboration, *Measurement of the muon stopping power in lead tungstate*, *2010 JINST* **5** P03007.
- [27] CMS collaboration, *CMS Physics: Technical Design Report*, CERN-LHCC-2006-001 (2006).

The CMS collaboration

Yerevan Physics Institute, Yerevan, Armenia

S. Chatrchyan, V. Khachatryan, A.M. Sirunyan

Institut für Hochenergiephysik der OeAW, Wien, Austria

W. Adam, B. Arnold, H. Bergauer, T. Bergauer, M. Dragicevic, M. Eichberger, J. Erö, M. Friedl, R. Frühwirth, V.M. Ghete, J. Hammer¹, S. Häsnel, M. Hoch, N. Hörmann, J. Hrubec, M. Jeitler, G. Kasieczka, K. Kastner, M. Krammer, D. Liko, I. Magrans de Abril, I. Mikulec, F. Mittermayr, B. Neuherz, M. Oberegger, M. Padrta, M. Pernicka, H. Rohringer, S. Schmid, R. Schöfbeck, T. Schreiner, R. Stark, H. Steininger, J. Strauss, A. Taurok, F. Teischinger, T. Themel, D. Uhl, P. Wagner, W. Waltenberger, G. Walzel, E. Widl, C.-E. Wulz

National Centre for Particle and High Energy Physics, Minsk, Belarus

V. Chekhovsky, O. Dvornikov, I. Emeliantchik, A. Litomin, V. Makarenko, I. Marfin, V. Mossolov, N. Shumeiko, A. Solin, R. Stefanovitch, J. Suarez Gonzalez, A. Tikhonov

Research Institute for Nuclear Problems, Minsk, Belarus

A. Fedorov, A. Karneyeu, M. Korzhik, V. Panov, R. Zuyevski

Research Institute of Applied Physical Problems, Minsk, Belarus

P. Kuchinsky

Universiteit Antwerpen, Antwerpen, Belgium

W. Beaumont, L. Benucci, M. Cardaci, E.A. De Wolf, E. Delmeire, D. Druzhkin, M. Hashemi, X. Janssen, T. Maes, L. Mucibello, S. Ochesanu, R. Rougny, M. Selvaggi, H. Van Haevermaet, P. Van Mechelen, N. Van Remortel

Vrije Universiteit Brussel, Brussel, Belgium

V. Adler, S. Beauceron, S. Blyweert, J. D'Hondt, S. De Weirdt, O. Devroede, J. Heyninck, A. Kalogeropoulos, J. Maes, M. Maes, M.U. Mozer, S. Tavernier, W. Van Doninck¹, P. Van Mulders, I. Vilella

Université Libre de Bruxelles, Bruxelles, Belgium

O. Bouhali, E.C. Chabert, O. Charaf, B. Clerboux, G. De Lentdecker, V. Dero, S. Elgammal, A.P.R. Gay, G.H. Hammad, P.E. Marage, S. Rugovac, C. Vander Velde, P. Vanlaer, J. Wickens

Ghent University, Ghent, Belgium

M. Grunewald, B. Klein, A. Marinov, D. Ryckbosch, F. Thyssen, M. Tytgat, L. Vanelderen, P. Verwilligen

Université Catholique de Louvain, Louvain-la-Neuve, Belgium

S. Basegmez, G. Bruno, J. Caudron, C. Delaere, P. Demin, D. Favart, A. Giammanco, G. Grégoire, V. Lemaitre, O. Militaru, S. Ovyn, K. Piotrkowski¹, L. Quertenmont, N. Schul

Université de Mons, Mons, Belgium

N. Beliy, E. Daubie

Centro Brasileiro de Pesquisas Fisicas, Rio de Janeiro, Brazil

G.A. Alves, M.E. Pol, M.H.G. Souza

Universidade do Estado do Rio de Janeiro, Rio de Janeiro, Brazil

W. Carvalho, D. De Jesus Damiao, C. De Oliveira Martins, S. Fonseca De Souza, L. Mundim, V. Oguri, A. Santoro, S.M. Silva Do Amaral, A. Sznajder

Instituto de Fisica Teorica, Universidade Estadual Paulista, Sao Paulo, Brazil

T.R. Fernandez Perez Tomei, M.A. Ferreira Dias, E. M. Gregores², S.F. Novaes

Institute for Nuclear Research and Nuclear Energy, Sofia, Bulgaria

K. Abadjiev¹, T. Anguelov, J. Damgov, N. Darmenov¹, L. Dimitrov, V. Genchev¹, P. Iaydjiev, S. Piperov, S. Stoykova, G. Sultanov, R. Trayanov, I. Vankov

University of Sofia, Sofia, Bulgaria

A. Dimitrov, M. Dyulendarova, V. Kozhuharov, L. Litov, E. Marinova, M. Mateev, B. Pavlov, P. Petkov, Z. Toteva¹

Institute of High Energy Physics, Beijing, China

G.M. Chen, H.S. Chen, W. Guan, C.H. Jiang, D. Liang, B. Liu, X. Meng, J. Tao, J. Wang, Z. Wang, Z. Xue, Z. Zhang

State Key Lab. of Nucl. Phys. and Tech., Peking University, Beijing, China

Y. Ban, J. Cai, Y. Ge, S. Guo, Z. Hu, Y. Mao, S.J. Qian, H. Teng, B. Zhu

Universidad de Los Andes, Bogota, Colombia

C. Avila, M. Baquero Ruiz, C.A. Carrillo Montoya, A. Gomez, B. Gomez Moreno, A.A. Ocampo Rios, A.F. Osorio Oliveros, D. Reyes Romero, J.C. Sanabria

Technical University of Split, Split, Croatia

N. Godinovic, K. Lelas, R. Plestina, D. Polic, I. Puljak

University of Split, Split, Croatia

Z. Antunovic, M. Dzelalija

Institute Rudjer Boskovic, Zagreb, Croatia

V. Brigljevic, S. Duric, K. Kadija, S. Morovic

University of Cyprus, Nicosia, Cyprus

R. Fereos, M. Galanti, J. Mousa, A. Papadakis, F. Ptochos, P.A. Razis, D. Tsiakkouri, Z. Zinonos

National Institute of Chemical Physics and Biophysics, Tallinn, Estonia

A. Hektor, M. Kadastik, K. Kannike, M. Müntel, M. Raidal, L. Rebane

Helsinki Institute of Physics, Helsinki, Finland

E. Anttila, S. Czellar, J. Härkönen, A. Heikkinen, V. Karimäki, R. Kinnunen, J. Klem, M.J. Kortelainen, T. Lampén, K. Lassila-Perini, S. Lehti, T. Lindén, P. Luukka, T. Mäenpää, J. Nysten, E. Tuominen, J. Tuominiemi, D. Ungaro, L. Wendland

Lappeenranta University of Technology, Lappeenranta, Finland

K. Banzuzi, A. Korpela, T. Tuuva

Laboratoire d'Annecy-le-Vieux de Physique des Particules, IN2P3-CNRS, Annecy-le-Vieux, France

P. Nedelec, D. Sillou

DSM/IRFU, CEA/Saclay, Gif-sur-Yvette, France

M. Besancon, R. Chipaux, M. Dejardin, D. Denegri, J. Descamps, B. Fabbro, J.L. Faure, F. Ferri, S. Ganjour, F.X. Gentit, A. Givernaud, P. Gras, G. Hamel de Monchenault, P. Jarry, M.C. Lemaire, E. Locci, J. Malcles, M. Marionneau, L. Millischer, J. Rander, A. Rosowsky, D. Rousseau, M. Titov, P. Verrecchia

Laboratoire Leprince-Ringuet, Ecole Polytechnique, IN2P3-CNRS, Palaiseau, France

S. Baffioni, L. Bianchini, M. Bluj³, P. Busson, C. Charlot, L. Dobrzynski, R. Granier de Cassagnac, M. Haguenaue, P. Miné, P. Paganini, Y. Sirois, C. Thiebaux, A. Zabi

Institut Pluridisciplinaire Hubert Curien, Université de Strasbourg, Université de Haute Alsace Mulhouse, CNRS/IN2P3, Strasbourg, France

J.-L. Agram⁴, A. Besson, D. Bloch, D. Bodin, J.-M. Brom, E. Conte⁴, F. Drouhin⁴, J.-C. Fontaine⁴, D. Gelé, U. Goerlach, L. Gross, P. Juillot, A.-C. Le Bihan, Y. Patois, J. Speck, P. Van Hove

Université de Lyon, Université Claude Bernard Lyon 1, CNRS-IN2P3, Institut de Physique Nucléaire de Lyon, Villeurbanne, France

C. Baty, M. Bedjidian, J. Blaha, G. Boudoul, H. Brun, N. Chanon, R. Chierici, D. Contardo, P. Depasse, T. Dupasquier, H. El Mamouni, F. Fassi⁵, J. Fay, S. Gascon, B. Ille, T. Kurca, T. Le Grand, M. Lethuillier, N. Lumb, L. Mirabito, S. Perries, M. Vander Donckt, P. Verdier

E. Andronikashvili Institute of Physics, Academy of Science, Tbilisi, Georgia

N. Djaoshvili, N. Roinishvili, V. Roinishvili

Institute of High Energy Physics and Informatization, Tbilisi State University, Tbilisi, Georgia

N. Amaglobeli

RWTH Aachen University, I. Physikalisches Institut, Aachen, Germany

R. Adolphi, G. Anagnostou, R. Brauer, W. Braunschweig, M. Edelhoff, H. Esser, L. Feld, W. Karpinski, A. Khomich, K. Klein, N. Mohr, A. Ostapchouk, D. Pandoulas, G. Pierschel, F. Raupach, S. Schael, A. Schultz von Dratzig, G. Schwering, D. Sprenger, M. Thomas, M. Weber, B. Wittmer, M. Wlochal

RWTH Aachen University, III. Physikalisches Institut A, Aachen, Germany

O. Actis, G. Altenhöfer, W. Bender, P. Biallass, M. Erdmann, G. Fetchenhauer¹, J. Frangenheim, T. Hebbeker, G. Hilgers, A. Hinzmann, K. Hoepfner, C. Hof, M. Kirsch, T. Klimkovich, P. Kreuzer¹, D. Lanske[†], M. Merschmeyer, A. Meyer, B. Philipps, H. Pieta, H. Reithler, S.A. Schmitz, L. Sonnenschein, M. Sowa, J. Steggemann, H. Szczesny, D. Teyssier, C. Zeidler

RWTH Aachen University, III. Physikalisches Institut B, Aachen, Germany

M. Bontenackels, M. Davids, M. Duda, G. Flügge, H. Geenen, M. Giffels, W. Haj Ahmad, T. Hermanns, D. Heydhausen, S. Kalinin, T. Kress, A. Linn, A. Nowack, L. Perchalla, M. Poettgens, O. Pooth, P. Sauerland, A. Stahl, D. Tornier, M.H. Zoeller

Deutsches Elektronen-Synchrotron, Hamburg, Germany

M. Aldaya Martin, U. Behrens, K. Borras, A. Campbell, E. Castro, D. Dammann, G. Eckerlin, A. Flossdorf, G. Flucke, A. Geiser, D. Hatton, J. Hauk, H. Jung, M. Kasemann, I. Katkov, C. Kleinwort, H. Kluge, A. Knutsson, E. Kuznetsova, W. Lange, W. Lohmann, R. Mankel¹,

M. Marienfeld, A.B. Meyer, S. Miglioranza, J. Mnich, M. Ohlerich, J. Olzem, A. Parenti, C. Rosemann, R. Schmidt, T. Schoerner-Sadenius, D. Volyanskyy, C. Wissing, W.D. Zeuner¹

University of Hamburg, Hamburg, Germany

C. Autermann, F. Bechtel, J. Draeger, D. Eckstein, U. Gebbert, K. Kaschube, G. Kaussen, R. Klanner, B. Mura, S. Naumann-Emme, F. Nowak, U. Pein, C. Sander, P. Schleper, T. Schum, H. Stadie, G. Steinbrück, J. Thomsen, R. Wolf

Institut für Experimentelle Kernphysik, Karlsruhe, Germany

J. Bauer, P. Blüm, V. Buege, A. Cakir, T. Chwalek, W. De Boer, A. Dierlamm, G. Dirkes, M. Feindt, U. Felzmann, M. Frey, A. Furgeri, J. Gruschke, C. Hackstein, F. Hartmann¹, S. Heier, M. Heinrich, H. Held, D. Hirschebuehl, K.H. Hoffmann, S. Honc, C. Jung, T. Kuhr, T. Liamsuwan, D. Martschei, S. Mueller, Th. Müller, M.B. Neuland, M. Niegel, O. Oberst, A. Oehler, J. Ott, T. Peiffer, D. Piparo, G. Quast, K. Rabbertz, F. Ratnikov, N. Ratnikova, M. Renz, C. Saout¹, G. Sartisoehn, A. Scheurer, P. Schieferdecker, F.-P. Schilling, G. Schott, H.J. Simonis, F.M. Stober, P. Sturm, D. Troendle, A. Trunov, W. Wagner, J. Wagner-Kuhr, M. Zeise, V. Zhukov⁶, E.B. Ziebarth

Institute of Nuclear Physics "Demokritos", Aghia Paraskevi, Greece

G. Daskalakis, T. Geralis, K. Karafasoulis, A. Kyriakis, D. Loukas, A. Markou, C. Markou, C. Mavrommatis, E. Petrakou, A. Zachariadou

University of Athens, Athens, Greece

L. Gouskos, P. Katsas, A. Panagiotou¹

University of Ioánnina, Ioánnina, Greece

I. Evangelou, P. Kokkas, N. Manthos, I. Papadopoulos, V. Patras, F.A. Triantis

KFKI Research Institute for Particle and Nuclear Physics, Budapest, Hungary

G. Bencze¹, L. Boldizsar, G. Debreczeni, C. Hajdu¹, S. Hernath, P. Hidas, D. Horvath⁷, K. Krajczar, A. Laszlo, G. Patay, F. Sikler, N. Toth, G. Vesztergombi

Institute of Nuclear Research ATOMKI, Debrecen, Hungary

N. Beni, G. Christian, J. Imrek, J. Molnar, D. Novak, J. Palinkas, G. Szekely, Z. Szillasi¹, K. Tokesi, V. Veszpremi

University of Debrecen, Debrecen, Hungary

A. Kapusi, G. Marian, P. Raics, Z. Szabo, Z.L. Trocsanyi, B. Ujvari, G. Zilizi

Panjab University, Chandigarh, India

S. Bansal, H.S. Bawa, S.B. Beri, V. Bhatnagar, M. Jindal, M. Kaur, R. Kaur, J.M. Kohli, M.Z. Mehta, N. Nishu, L.K. Saini, A. Sharma, A. Singh, J.B. Singh, S.P. Singh

University of Delhi, Delhi, India

S. Ahuja, S. Arora, S. Bhattacharya⁸, S. Chauhan, B.C. Choudhary, P. Gupta, S. Jain, S. Jain, M. Jha, A. Kumar, K. Ranjan, R.K. Shivpuri, A.K. Srivastava

Bhabha Atomic Research Centre, Mumbai, India

R.K. Choudhury, D. Dutta, S. Kailas, S.K. Kataria, A.K. Mohanty, L.M. Pant, P. Shukla, A. Topkar

Tata Institute of Fundamental Research - EHEP, Mumbai, India

T. Aziz, M. Guchait⁹, A. Gurtu, M. Maity¹⁰, D. Majumder, G. Majumder, K. Mazumdar, A. Nayak, A. Saha, K. Sudhakar

Tata Institute of Fundamental Research - HECR, Mumbai, India

S. Banerjee, S. Dugad, N.K. Mondal

Institute for Studies in Theoretical Physics & Mathematics (IPM), Tehran, Iran

H. Arfaei, H. Bakhshiansohi, A. Fahim, A. Jafari, M. Mohammadi Najafabadi, A. Moshaii, S. Paktinat Mehdiabadi, S. Rouhani, B. Safarzadeh, M. Zeinali

University College Dublin, Dublin, Ireland

M. Felcini

INFN Sezione di Bari ^a, Università di Bari ^b, Politecnico di Bari ^c, Bari, Italy

M. Abbrescia^{a,b}, L. Barbone^a, F. Chiumarulo^a, A. Clemente^a, A. Colaleo^a, D. Creanza^{a,c}, G. Cuscela^a, N. De Filippis^a, M. De Palma^{a,b}, G. De Robertis^a, G. Donvito^a, F. Fedele^a, L. Fiore^a, M. Franco^a, G. Iaselli^{a,c}, N. Lacalamita^a, F. Loddo^a, L. Lusito^{a,b}, G. Maggi^{a,c}, M. Maggi^a, N. Manna^{a,b}, B. Marangelli^{a,b}, S. My^{a,c}, S. Natali^{a,b}, S. Nuzzo^{a,b}, G. Papagni^a, S. Piccolomo^a, G.A. Pierro^a, C. Pinto^a, A. Pompili^{a,b}, G. Pugliese^{a,c}, R. Rajan^a, A. Ranieri^a, F. Romano^{a,c}, G. Roselli^{a,b}, G. Selvaggi^{a,b}, Y. Shinde^a, L. Silvestris^a, S. Tuppiti^{a,b}, G. Zito^a

INFN Sezione di Bologna ^a, Università di Bologna ^b, Bologna, Italy

G. Abbiendi^a, W. Bacchi^{a,b}, A.C. Benvenuti^a, M. Boldini^a, D. Bonacorsi^a, S. Braibant-Giacomelli^{a,b}, V.D. Cafaro^a, S.S. Caiazza^a, P. Capiluppi^{a,b}, A. Castro^{a,b}, F.R. Cavallo^a, G. Codispoti^{a,b}, M. Cuffiani^{a,b}, I. D'Antone^a, G.M. Dallavalle^{a,1}, F. Fabbri^a, A. Fanfani^{a,b}, D. Fasanella^a, P. Giacomelli^a, V. Giordano^a, M. Giunta^{a,1}, C. Grandi^a, M. Guerzoni^a, S. Marcellini^a, G. Masetti^{a,b}, A. Montanari^a, F.L. Navarria^{a,b}, F. Odorici^a, G. Pellegrini^a, A. Perrotta^a, A.M. Rossi^{a,b}, T. Rovelli^{a,b}, G. Siroli^{a,b}, G. Torromeo^a, R. Travaglini^{a,b}

INFN Sezione di Catania ^a, Università di Catania ^b, Catania, Italy

S. Albergo^{a,b}, S. Costa^{a,b}, R. Potenza^{a,b}, A. Tricomi^{a,b}, C. Tuve^a

INFN Sezione di Firenze ^a, Università di Firenze ^b, Firenze, Italy

G. Barbagli^a, G. Broccolo^{a,b}, V. Ciulli^{a,b}, C. Civinini^a, R. D'Alessandro^{a,b}, E. Focardi^{a,b}, S. Frosali^{a,b}, E. Gallo^a, C. Genta^{a,b}, G. Landi^{a,b}, P. Lenzi^{a,b,1}, M. Meschini^a, S. Paoletti^a, G. Sguazzoni^a, A. Tropiano^a

INFN Laboratori Nazionali di Frascati, Frascati, Italy

L. Benussi, M. Bertani, S. Bianco, S. Colafranceschi¹¹, D. Colonna¹¹, F. Fabbri, M. Giardoni, L. Passamonti, D. Piccolo, D. Pierluigi, B. Ponzio, A. Russo

INFN Sezione di Genova, Genova, Italy

P. Fabbricatore, R. Musenich

INFN Sezione di Milano-Bicocca ^a, Università di Milano-Bicocca ^b, Milano, Italy

A. Benaglia^a, M. Calloni^a, G.B. Cerati^{a,b,1}, P. D'Angelo^a, F. De Guio^a, F.M. Farina^a, A. Ghezzi^a, P. Govoni^{a,b}, M. Malberti^{a,b,1}, S. Malvezzi^a, A. Martelli^a, D. Menasce^a, V. Miccio^{a,b}, L. Moroni^a, P. Negri^{a,b}, M. Paganoni^{a,b}, D. Pedrini^a, A. Pullia^{a,b}, S. Ragazzi^{a,b}, N. Redaelli^a, S. Sala^a, R. Salerno^{a,b}, T. Tabarelli de Fatis^{a,b}, V. Tancini^{a,b}, S. Taroni^{a,b}

INFN Sezione di Napoli ^a, Università di Napoli "Federico II" ^b, Napoli, Italy

S. Buontempo^a, N. Cavallo^a, A. Cimmino^{a,b,1}, M. De Gruttola^{a,b,1}, F. Fabozzi^{a,12}, A.O.M. Iorio^a, L. Lista^a, D. Lomidze^a, P. Noli^{a,b}, P. Paolucci^a, C. Sciacca^{a,b}

INFN Sezione di Padova ^a, Università di Padova ^b, Padova, Italy

P. Azzi^{a,1}, N. Bacchetta^a, L. Barcellan^a, P. Bellan^{a,b,1}, M. Bellato^a, M. Benettoni^a, M. Biasotto^{a,13}, D. Bisello^{a,b}, E. Borsato^{a,b}, A. Branca^a, R. Carlin^{a,b}, L. Castellani^a, P. Checchia^a, E. Conti^a, F. Dal Corso^a, M. De Mattia^{a,b}, T. Dorigo^a, U. Dosselli^a, F. Fanzago^a, F. Gasparini^{a,b}, U. Gasparini^{a,b}, P. Giubilato^{a,b}, F. Gonella^a, A. Gresele^{a,14}, M. Gulmini^{a,13}, A. Kaminskiy^{a,b}, S. Lacaprara^{a,13}, I. Lazzizzera^{a,14}, M. Margoni^{a,b}, G. Maron^{a,13}, S. Mattiazzo^{a,b}, M. Mazzucato^a, M. Meneghelli^a, A.T. Meneguzzo^{a,b}, M. Michelotto^a, F. Montecassiano^a, M. Nespolo^a, M. Passaseo^a, M. Pegoraro^a, L. Perrozzi^a, N. Pozzobon^{a,b}, P. Ronchese^{a,b}, F. Simonetto^{a,b}, N. Toniolo^a, E. Torassa^a, M. Tosi^{a,b}, A. Triossi^a, S. Vanini^{a,b}, S. Ventura^a, P. Zotto^{a,b}, G. Zumerle^{a,b}

INFN Sezione di Pavia ^a, Università di Pavia ^b, Pavia, Italy

P. Baesso^{a,b}, U. Berzano^a, S. Bricola^a, M.M. Necchi^{a,b}, D. Pagano^{a,b}, S.P. Ratti^{a,b}, C. Riccardi^{a,b}, P. Torre^{a,b}, A. Vicini^a, P. Vitulo^{a,b}, C. Viviani^{a,b}

INFN Sezione di Perugia ^a, Università di Perugia ^b, Perugia, Italy

D. Aisa^a, S. Aisa^a, E. Babucci^a, M. Biasini^{a,b}, G.M. Bilei^a, B. Caponeri^{a,b}, B. Checcucci^a, N. Dinu^a, L. Fanò^a, L. Farnesini^a, P. Lariccia^{a,b}, A. Lucaroni^{a,b}, G. Mantovani^{a,b}, A. Nappi^{a,b}, A. Piluso^a, V. Postolache^a, A. Santocchia^{a,b}, L. Servoli^a, D. Tonoiu^a, A. Vedae^a, R. Volpe^{a,b}

INFN Sezione di Pisa ^a, Università di Pisa ^b, Scuola Normale Superiore di Pisa ^c, Pisa, Italy

P. Azzurri^{a,c}, G. Bagliesi^a, J. Bernardini^{a,b}, L. Berretta^a, T. Boccali^a, A. Bocci^{a,c}, L. Borrello^{a,c}, F. Bosi^a, F. Calzolari^a, R. Castaldi^a, R. Dell'Orso^a, F. Fiori^{a,b}, L. Foà^{a,c}, S. Gennai^{a,c}, A. Giassi^a, A. Kraan^a, F. Ligabue^{a,c}, T. Lomtadze^a, F. Mariani^a, L. Martini^a, M. Massa^a, A. Messineo^{a,b}, A. Moggi^a, F. Palla^a, F. Palmonari^a, G. Petraghani^a, G. Petrucciani^{a,c}, F. Raffaelli^a, S. Sarkar^a, G. Segneri^a, A.T. Serban^a, P. Spagnolo^{a,1}, R. Tenchini^{a,1}, S. Tolaini^a, G. Tonelli^{a,b,1}, A. Venturi^a, P.G. Verdini^a

INFN Sezione di Roma ^a, Università di Roma "La Sapienza" ^b, Roma, Italy

S. Baccaro^{a,15}, L. Barone^{a,b}, A. Bartoloni^a, F. Cavallari^{a,1}, I. Dafinei^a, D. Del Re^{a,b}, E. Di Marco^{a,b}, M. Diemoz^a, D. Franci^{a,b}, E. Longo^{a,b}, G. Organtini^{a,b}, A. Palma^{a,b}, F. Pandolfi^{a,b}, R. Paramatti^{a,1}, F. Pellegrino^a, S. Rahatlou^{a,b}, C. Rovelli^a

INFN Sezione di Torino ^a, Università di Torino ^b, Università del Piemonte Orientale (Novara) ^c, Torino, Italy

G. Alampi^a, N. Amapane^{a,b}, R. Arcidiacono^{a,b}, S. Argiro^{a,b}, M. Arneodo^{a,c}, C. Biino^a, M.A. Borgia^{a,b}, C. Botta^{a,b}, N. Cartiglia^a, R. Castello^{a,b}, G. Cerminara^{a,b}, M. Costa^{a,b}, D. Dattola^a, G. Dellacasa^a, N. Demaria^a, G. Dughera^a, F. Dumitrache^a, A. Graziano^{a,b}, C. Mariotti^a, M. Marone^{a,b}, S. Maselli^a, E. Migliore^{a,b}, G. Mila^{a,b}, V. Monaco^{a,b}, M. Musich^{a,b}, M. Nervo^{a,b}, M.M. Obertino^{a,c}, S. Oggero^{a,b}, R. Panero^a, N. Pastrone^a, M. Pelliccioni^{a,b}, A. Romero^{a,b}, M. Ruspa^{a,c}, R. Sacchi^{a,b}, A. Solano^{a,b}, A. Staiano^a, P.P. Trapani^{a,b,1}, D. Trocino^{a,b}, A. Vilela Pereira^{a,b}, L. Visca^{a,b}, A. Zampieri^a

INFN Sezione di Trieste ^a, Università di Trieste ^b, Trieste, Italy

F. Ambroglini^{a,b}, S. Belforte^a, F. Cossutti^a, G. Della Ricca^{a,b}, B. Gobbo^a, A. Penzo^a

Kyungpook National University, Daegu, Korea

S. Chang, J. Chung, D.H. Kim, G.N. Kim, D.J. Kong, H. Park, D.C. Son

Wonkwang University, Iksan, Korea

S.Y. Bahk

Chonnam National University, Kwangju, Korea

S. Song

Konkuk University, Seoul, Korea

S.Y. Jung

Korea University, Seoul, Korea

B. Hong, H. Kim, J.H. Kim, K.S. Lee, D.H. Moon, S.K. Park, H.B. Rhee, K.S. Sim

Seoul National University, Seoul, Korea

J. Kim

University of Seoul, Seoul, Korea

M. Choi, G. Hahn, I.C. Park

Sungkyunkwan University, Suwon, Korea

S. Choi, Y. Choi, J. Goh, H. Jeong, T.J. Kim, J. Lee, S. Lee

Vilnius University, Vilnius, Lithuania

M. Janulis, D. Martisiute, P. Petrov, T. Sabonis

Centro de Investigacion y de Estudios Avanzados del IPN, Mexico City, MexicoH. Castilla Valdez¹, A. Sánchez Hernández**Universidad Iberoamericana, Mexico City, Mexico**

S. Carrillo Moreno

Universidad Autónoma de San Luis Potosí, San Luis Potosí, Mexico

A. Morelos Pineda

University of Auckland, Auckland, New Zealand

P. Allfrey, R.N.C. Gray, D. Krofcheck

University of Canterbury, Christchurch, New Zealand

N. Bernardino Rodrigues, P.H. Butler, T. Signal, J.C. Williams

National Centre for Physics, Quaid-I-Azam University, Islamabad, Pakistan

M. Ahmad, I. Ahmed, W. Ahmed, M.I. Asghar, M.I.M. Awan, H.R. Hoorani, I. Hussain, W.A. Khan, T. Khurshid, S. Muhammad, S. Qazi, H. Shahzad

Institute of Experimental Physics, Warsaw, PolandM. Cwiok, R. Dabrowski, W. Dominik, K. Doroba, M. Konecki, J. Krolikowski, K. Pozniak¹⁶, R. Romaniuk, W. Zabolotny¹⁶, P. Zych**Soltan Institute for Nuclear Studies, Warsaw, Poland**

T. Frueboes, R. Gokieli, L. Gosciolo, M. Górski, M. Kazana, K. Nawrocki, M. Szleper, G. Wrochna, P. Zalewski

Laboratório de Instrumentação e Física Experimental de Partículas, Lisboa, Portugal

N. Almeida, L. Antunes Pedro, P. Bargassa, A. David, P. Faccioli, P.G. Ferreira Parracho, M. Freitas Ferreira, M. Gallinaro, M. Guerra Jordao, P. Martins, G. Mini, P. Musella, J. Pela, L. Raposo, P.Q. Ribeiro, S. Sampaio, J. Seixas, J. Silva, P. Silva, D. Soares, M. Sousa, J. Varela, H.K. Wöhri

Joint Institute for Nuclear Research, Dubna, Russia

I. Altsybeev, I. Belotelov, P. Bunin, Y. Ershov, I. Filozova, M. Finger, M. Finger Jr., A. Golunov, I. Golutvin, N. Gorbounov, V. Kalagin, A. Kamenev, V. Karjavin, V. Konoplyanikov, V. Korenkov, G. Kozlov, A. Kurenkov, A. Lanev, A. Makankin, V.V. Mitsyn, P. Moisezenz, E. Nikonov, D. Oleynik, V. Palichik, V. Perelygin, A. Petrosyan, R. Semenov, S. Shmatov, V. Smirnov, D. Smolin, E. Tikhonenko, S. Vasil'ev, A. Vishnevskiy, A. Volodko, A. Zarubin, V. Zhiltsov

Petersburg Nuclear Physics Institute, Gatchina (St Petersburg), Russia

N. Bondar, L. Chtchipounov, A. Denisov, Y. Gavrikov, G. Gavrillov, V. Golovtsov, Y. Ivanov, V. Kim, V. Kozlov, P. Levchenko, G. Obrant, E. Orishchin, A. Petrunin, Y. Shcheglov, A. Shchetkovskiy, V. Sknar, I. Smirnov, V. Sulimov, V. Tarakanov, L. Uvarov, S. Vavilov, G. Velichko, S. Volkov, A. Vorobyev

Institute for Nuclear Research, Moscow, Russia

Yu. Andreev, A. Anisimov, P. Antipov, A. Dermenev, S. Gninenko, N. Golubev, M. Kirsanov, N. Krasnikov, V. Matveev, A. Pashenkov, V.E. Postoev, A. Solovey, A. Solovey, A. Toropin, S. Troitsky

Institute for Theoretical and Experimental Physics, Moscow, Russia

A. Baud, V. Epshteyn, V. Gavrillov, N. Ilina, V. Kaftanov[†], V. Kolosov, M. Kossov¹, A. Krokhotin, S. Kuleshov, A. Oulianov, G. Safronov, S. Semenov, I. Shreyber, V. Stolin, E. Vlasov, A. Zhokin

Moscow State University, Moscow, Russia

E. Boos, M. Dubinin¹⁷, L. Dudko, A. Ershov, A. Gribushin, V. Klyukhin, O. Kodolova, I. Lokhtin, S. Petrushanko, L. Sarycheva, V. Savrin, A. Snigirev, I. Vardanyan

P.N. Lebedev Physical Institute, Moscow, Russia

I. Dremin, M. Kirakosyan, N. Konovalova, S.V. Rusakov, A. Vinogradov

State Research Center of Russian Federation, Institute for High Energy Physics, Protvino, Russia

S. Akimenko, A. Artamonov, I. Azhgirey, S. Bitioukov, V. Burtovoy, V. Grishin¹, V. Kachanov, D. Konstantinov, V. Krychkine, A. Levine, I. Lobov, V. Lukanin, Y. Mel'nik, V. Petrov, R. Ryutin, S. Slabospitsky, A. Sobol, A. Sytine, L. Tourtchanovitch, S. Troshin, N. Tyurin, A. Uzunian, A. Volkov

Vinca Institute of Nuclear Sciences, Belgrade, Serbia

P. Adzic, M. Djordjevic, D. Jovanovic¹⁸, D. Krpic¹⁸, D. Maletic, J. Puzovic¹⁸, N. Smiljkovic

Centro de Investigaciones Energéticas Medioambientales y Tecnológicas (CIEMAT), Madrid, Spain

M. Aguilar-Benitez, J. Alberdi, J. Alcaraz Maestre, P. Arce, J.M. Barcala, C. Battilana, C. Burgos Lazaro, J. Caballero Bejar, E. Calvo, M. Cardenas Montes, M. Cepeda, M. Cerrada, M. Chamizo Llatas, F. Clemente, N. Colino, M. Daniel, B. De La Cruz, A. Delgado Peris, C. Diez Pardos, C. Fernandez Bedoya, J.P. Fernández Ramos, A. Ferrando, J. Flix, M.C. Fouz, P. Garcia-Abia, A.C. Garcia-Bonilla, O. Gonzalez Lopez, S. Goy Lopez, J.M. Hernandez, M.I. Josa, J. Marin, G. Merino, J. Molina, A. Molinero, J.J. Navarrete, J.C. Oller, J. Puerta Pelayo, L. Romero, J. Santaolalla, C. Villanueva Munoz, C. Willmott, C. Yuste

Universidad Autónoma de Madrid, Madrid, Spain

C. Albajar, M. Blanco Otano, J.F. de Trocóniz, A. García Raboso, J.O. Lopez Berengueres

Universidad de Oviedo, Oviedo, Spain

J. Cuevas, J. Fernandez Menendez, I. Gonzalez Caballero, L. Lloret Iglesias, H. Naves Sordo, J.M. Vizan Garcia

Instituto de Física de Cantabria (IFCA), CSIC-Universidad de Cantabria, Santander, Spain

I.J. Cabrillo, A. Calderon, S.H. Chuang, I. Diaz Merino, C. Diez Gonzalez, J. Duarte Campderros, M. Fernandez, G. Gomez, J. Gonzalez Sanchez, R. Gonzalez Suarez, C. Jorda, P. Lobelle Pardo, A. Lopez Virto, J. Marco, R. Marco, C. Martinez Rivero, P. Martinez Ruiz del Arbol, F. Matorras, T. Rodrigo, A. Ruiz Jimeno, L. Scodellaro, M. Sobron Sanudo, I. Vila, R. Vilar Cortabitarte

CERN, European Organization for Nuclear Research, Geneva, Switzerland

D. Abbaneo, E. Albert, M. Alidra, S. Ashby, E. Auffray, J. Baechler, P. Baillon, A.H. Ball, S.L. Bally, D. Barney, F. Beaudette¹⁹, R. Bellan, D. Benedetti, G. Benelli, C. Bernet, P. Bloch, S. Bolognesi, M. Bona, J. Bos, N. Bourgeois, T. Bourrel, H. Breuker, K. Bunkowski, D. Campi, T. Camporesi, E. Cano, A. Cattai, J.P. Chatelain, M. Chauvey, T. Christiansen, J.A. Coarasa Perez, A. Conde Garcia, R. Covarelli, B. Curé, A. De Roeck, V. Delachenal, D. Deyrail, S. Di Vincenzo²⁰, S. Dos Santos, T. Dupont, L.M. Edera, A. Elliott-Peisert, M. Eppard, M. Favre, N. Frank, W. Funk, A. Gaddi, M. Gastal, M. Gateau, H. Gerwig, D. Gigi, K. Gill, D. Giordano, J.P. Girod, F. Glege, R. Gomez-Reino Garrido, R. Goudard, S. Gowdy, R. Guida, L. Guiducci, J. Gutleber, M. Hansen, C. Hartl, J. Harvey, B. Hegner, H.F. Hoffmann, A. Holzner, A. Honma, M. Huhtinen, V. Innocente, P. Janot, G. Le Godec, P. Lecoq, C. Leonidopoulos, R. Loos, C. Lourenço, A. Lyonnet, A. Macpherson, N. Magini, J.D. Maillefaud, G. Maire, T. Mäki, L. Malgeri, M. Mannelli, L. Masetti, F. Meijers, P. Meridiani, S. Mersi, E. Meschi, A. Meynet Cordonnier, R. Moser, M. Mulders, J. Mulon, M. Noy, A. Oh, G. Olesen, A. Onnela, T. Orimoto, L. Orsini, E. Perez, G. Perinic, J.F. Pernot, P. Petagna, P. Petiot, A. Petrilli, A. Pfeiffer, M. Pierini, M. Pimiä, R. Pintus, B. Pirollet, H. Postema, A. Racz, S. Ravat, S.B. Rew, J. Rodrigues Antunes, G. Rolandi²¹, M. Rovere, V. Ryjov, H. Sakulin, D. Samyn, H. Sauce, C. Schäfer, W.D. Schlatter, M. Schröder, C. Schwick, A. Sciaba, I. Segoni, A. Sharma, N. Siegrist, P. Siegrist, N. Sinanis, T. Sobrier, P. Sphicas²², D. Spiga, M. Spiropulu¹⁷, F. Stöckli, P. Traczyk, P. Tropea, J. Troska, A. Tsirou, L. Veillet, G.I. Veres, M. Voutilainen, P. Wertelaers, M. Zanetti

Paul Scherrer Institut, Villigen, Switzerland

W. Bertl, K. Deiters, W. Erdmann, K. Gabathuler, R. Horisberger, Q. Ingram, H.C. Kaestli, S. König, D. Kotlinski, U. Langenegger, F. Meier, D. Renker, T. Rohe, J. Sibille²³, A. Starodumov²⁴

Institute for Particle Physics, ETH Zurich, Zurich, Switzerland

B. Betev, L. Caminada²⁵, Z. Chen, S. Cittolin, D.R. Da Silva Di Calafiori, S. Dambach²⁵, G. Dissertori, M. Dittmar, C. Eggel²⁵, J. Eugster, G. Faber, K. Freudenreich, C. Grab, A. Hervé, W. Hintz, P. Lecomte, P.D. Luckey, W. Lustermann, C. Marchica²⁵, P. Milenovic²⁶, F. Moortgat, A. Nardulli, F. Nessi-Tedaldi, L. Pape, F. Pauss, T. Punz, A. Rizzi, F.J. Ronga, L. Sala, A.K. Sanchez, M.-C. Sawley, V. Sordini, B. Stieger, L. Tauscher[†], A. Thea, K. Theofilatos, D. Treille, P. Trüb²⁵, M. Weber, L. Wehrli, J. Weng, S. Zelepoukine²⁷

Universität Zürich, Zurich, Switzerland

C. Amsler, V. Chiochia, S. De Visscher, C. Regenfus, P. Robmann, T. Rommerskirchen, A. Schmidt, D. Tsirigkas, L. Wilke

National Central University, Chung-Li, Taiwan

Y.H. Chang, E.A. Chen, W.T. Chen, A. Go, C.M. Kuo, S.W. Li, W. Lin

National Taiwan University (NTU), Taipei, Taiwan

P. Bartalini, P. Chang, Y. Chao, K.F. Chen, W.-S. Hou, Y. Hsiung, Y.J. Lei, S.W. Lin, R.-S. Lu, J. Schümann, J.G. Shiu, Y.M. Tzeng, K. Ueno, Y. Velikzhanin, C.C. Wang, M. Wang

Cukurova University, Adana, Turkey

A. Adiguzel, A. Ayhan, A. Azman Gokce, M.N. Bakirci, S. Cerci, I. Dumanoglu, E. Eskut, S. Girgis, E. Gurpinar, I. Hos, T. Karaman, T. Karaman, A. Kayis Topaksu, P. Kurt, G. Önengüt, G. Önengüt Gökbulut, K. Ozdemir, S. Ozturk, A. Polatöz, K. Sogut²⁸, B. Tali, H. Topakli, D. Uzun, L.N. Vergili, M. Vergili

Middle East Technical University, Physics Department, Ankara, Turkey

I.V. Akin, T. Aliev, S. Bilmis, M. Deniz, H. Gamsizkan, A.M. Guler, K. Öcalan, M. Serin, R. Sever, U.E. Surat, M. Zeyrek

Bogaçi University, Department of Physics, Istanbul, Turkey

M. Deliomeroglu, D. Demir²⁹, E. Gülmez, A. Halu, B. Isildak, M. Kaya³⁰, O. Kaya³⁰, S. Ozkorucuklu³¹, N. Sonmez³²

National Scientific Center, Kharkov Institute of Physics and Technology, Kharkov, Ukraine

L. Levchuk, S. Lukyanenko, D. Soroka, S. Zub

University of Bristol, Bristol, United Kingdom

F. Bostock, J.J. Brooke, T.L. Cheng, D. Cussans, R. Frazier, J. Goldstein, N. Grant, M. Hansen, G.P. Heath, H.F. Heath, C. Hill, B. Huckvale, J. Jackson, C.K. Mackay, S. Metson, D.M. Newbold³³, K. Nirunpong, V.J. Smith, J. Velthuis, R. Walton

Rutherford Appleton Laboratory, Didcot, United Kingdom

K.W. Bell, C. Brew, R.M. Brown, B. Camanzi, D.J.A. Cockerill, J.A. Coughlan, N.I. Geddes, K. Harder, S. Harper, B.W. Kennedy, P. Murray, C.H. Shepherd-Themistocleous, I.R. Tomalin, J.H. Williams[†], W.J. Womersley, S.D. Worm

Imperial College, University of London, London, United Kingdom

R. Bainbridge, G. Ball, J. Ballin, R. Beuselinck, O. Buchmuller, D. Colling, N. Cripps, G. Davies, M. Della Negra, C. Foudas, J. Fulcher, D. Futyan, G. Hall, J. Hays, G. Iles, G. Karapostoli, B.C. MacEvoy, A.-M. Magnan, J. Marrouche, J. Nash, A. Nikitenko²⁴, A. Papageorgiou, M. Pesaresi, K. Petridis, M. Pioppi³⁴, D.M. Raymond, N. Rompotis, A. Rose, M.J. Ryan, C. Seez, P. Sharp, G. Sidiropoulos¹, M. Stettler, M. Stoye, M. Takahashi, A. Tapper, C. Timlin, S. Tourneur, M. Vazquez Acosta, T. Virdee¹, S. Wakefield, D. Wardrope, T. Whyntie, M. Wingham

Brunel University, Uxbridge, United Kingdom

J.E. Cole, I. Goitom, P.R. Hobson, A. Khan, P. Kyberd, D. Leslie, C. Munro, I.D. Reid, C. Siamitros, R. Taylor, L. Teodorescu, I. Yaselli

Boston University, Boston, U.S.A.

T. Bose, M. Carleton, E. Hazen, A.H. Heering, A. Heister, J. St. John, P. Lawson, D. Lazic, D. Osborne, J. Rohlf, L. Sulak, S. Wu

Brown University, Providence, U.S.A.

J. Andrea, A. Avetisyan, S. Bhattacharya, J.P. Chou, D. Cutts, S. Esen, G. Kukartsev, G. Landsberg, M. Narain, D. Nguyen, T. Speer, K.V. Tsang

University of California, Davis, Davis, U.S.A.

R. Breedon, M. Calderon De La Barca Sanchez, M. Case, D. Cebra, M. Chertok, J. Conway, P.T. Cox, J. Dolen, R. Erbacher, E. Friis, W. Ko, A. Kopecky, R. Lander, A. Lister, H. Liu, S. Maruyama, T. Miceli, M. Nikolic, D. Pellett, J. Robles, M. Searle, J. Smith, M. Squires, J. Stilley, M. Tripathi, R. Vasquez Sierra, C. Veelken

University of California, Los Angeles, Los Angeles, U.S.A.

V. Andreev, K. Arisaka, D. Cline, R. Cousins, S. Erhan¹, J. Hauser, M. Ignatenko, C. Jarvis, J. Mumford, C. Plager, G. Rakness, P. Schlein[†], J. Tucker, V. Valuev, R. Wallny, X. Yang

University of California, Riverside, Riverside, U.S.A.

J. Babb, M. Bose, A. Chandra, R. Clare, J.A. Ellison, J.W. Gary, G. Hanson, G.Y. Jeng, S.C. Kao, F. Liu, H. Liu, A. Luthra, H. Nguyen, G. Pasztor³⁵, A. Satpathy, B.C. Shen[†], R. Stringer, J. Sturdy, V. Sytnik, R. Wilken, S. Wimpenny

University of California, San Diego, La Jolla, U.S.A.

J.G. Branson, E. Dusinger, D. Evans, F. Golf, R. Kelley, M. Lebourgeois, J. Letts, E. Lipeles, B. Mangano, J. Muelmenstaedt, M. Norman, S. Padhi, A. Petrucci, H. Pi, M. Pieri, R. Ranieri, M. Sani, V. Sharma, S. Simon, F. Würthwein, A. Yagil

University of California, Santa Barbara, Santa Barbara, U.S.A.

C. Campagnari, M. D'Alfonso, T. Danielson, J. Garberson, J. Incandela, C. Justus, P. Kalavase, S.A. Koay, D. Kovalskyi, V. Krutelyov, J. Lamb, S. Lowette, V. Pavlunin, F. Rebassoo, J. Ribnik, J. Richman, R. Rossin, D. Stuart, W. To, J.R. Vlimant, M. Witherell

California Institute of Technology, Pasadena, U.S.A.

A. Apresyan, A. Bornheim, J. Bunn, M. Chiorboli, M. Gataullin, D. Kcira, V. Litvine, Y. Ma, H.B. Newman, C. Rogan, V. Timciuc, J. Veverka, R. Wilkinson, Y. Yang, L. Zhang, K. Zhu, R.Y. Zhu

Carnegie Mellon University, Pittsburgh, U.S.A.

B. Akgun, R. Carroll, T. Ferguson, D.W. Jang, S.Y. Jun, M. Paulini, J. Russ, N. Terentyev, H. Vogel, I. Vorobiev

University of Colorado at Boulder, Boulder, U.S.A.

J.P. Cumalat, M.E. Dinardo, B.R. Drell, W.T. Ford, B. Heyburn, E. Luiggi Lopez, U. Nauenberg, K. Stenson, K. Ulmer, S.R. Wagner, S.L. Zang

Cornell University, Ithaca, U.S.A.

L. Agostino, J. Alexander, F. Blekman, D. Cassel, A. Chatterjee, S. Das, L.K. Gibbons, B. Heltsley, W. Hopkins, A. Khukhunaishvili, B. Kreis, V. Kuznetsov, J.R. Patterson, D. Puigh, A. Ryd, X. Shi, S. Stroiney, W. Sun, W.D. Teo, J. Thom, J. Vaughan, Y. Weng, P. Wittich

Fairfield University, Fairfield, U.S.A.

C.P. Beetz, G. Cirino, C. Sanzeni, D. Winn

Fermi National Accelerator Laboratory, Batavia, U.S.A.

S. Abdullin, M.A. Afaq¹, M. Albrow, B. Ananthan, G. Apollinari, M. Atac, W. Badgett, L. Bagby, J.A. Bakken, B. Baldin, S. Banerjee, K. Banicz, L.A.T. Bauerdick, A. Beretvas, J. Berryhill, P.C. Bhat, K. Biery, M. Binkley, I. Bloch, F. Borcherding, A.M. Brett, K. Burkett, J.N. Butler, V. Chetluru, H.W.K. Cheung, F. Chlebana, I. Churin, S. Cihangir, M. Crawford, W. Dagenhart, M. Demarteau, G. Derylo, D. Dykstra, D.P. Eartly, J.E. Elias, V.D. Elvira, D. Evans, L. Feng, M. Fischler, I. Fisk, S. Foulkes, J. Freeman, P. Gartung, E. Gottschalk, T. Grassi, D. Green, Y. Guo, O. Gutsche, A. Hahn, J. Hanlon, R.M. Harris, B. Holzman, J. Howell, D. Hufnagel, E. James, H. Jensen, M. Johnson, C.D. Jones, U. Joshi, E. Juska, J. Kaiser, B. Klima, S. Kossiakov, K. Kousouris, S. Kwan, C.M. Lei, P. Limon, J.A. Lopez Perez, S. Los, L. Lueking, G. Lukhanin, S. Lusin¹, J. Lykken, K. Maeshima, J.M. Marraffino, D. Mason, P. McBride, T. Miao, K. Mishra, S. Moccia, R. Mommsen, S. Mrenna, A.S. Muhammad, C. Newman-Holmes, C. Noeding, V. O'Dell, O. Prokofyev, R. Rivera, C.H. Rivetta, A. Ronzhin, P. Rossman, S. Ryu, V. Sekhri, E. Sexton-Kennedy, I. Sfiligoi, S. Sharma, T.M. Shaw, D. Shpakov, E. Skup, R.P. Smith[†], A. Soha, W.J. Spalding, L. Spiegel, I. Suzuki, P. Tan, W. Tanenbaum, S. Tkaczyk¹, R. Trentadue¹, L. Uplegger, E.W. Vaandering, R. Vidal, J. Whitmore, E. Wicklund, W. Wu, J. Yarba, F. Yumiceva, J.C. Yun

University of Florida, Gainesville, U.S.A.

D. Acosta, P. Avery, V. Barashko, D. Bourilkov, M. Chen, G.P. Di Giovanni, D. Dobur, A. Drozdetskiy, R.D. Field, Y. Fu, I.K. Furic, J. Gartner, D. Holmes, B. Kim, S. Klimenko, J. Konigsberg, A. Korytov, K. Kotov, A. Kropivnitskaya, T. Kypreos, A. Madorsky, K. Matchev, G. Mitselmakher, Y. Pakhotin, J. Piedra Gomez, C. Prescott, V. Rapsevicius, R. Remington, M. Schmitt, B. Scurlock, D. Wang, J. Yelton

Florida International University, Miami, U.S.A.

C. Ceron, V. Gaultney, L. Kramer, L.M. Lebolo, S. Linn, P. Markowitz, G. Martinez, J.L. Rodriguez

Florida State University, Tallahassee, U.S.A.

T. Adams, A. Askew, H. Baer, M. Bertoldi, J. Chen, W.G.D. Dharmaratna, S.V. Gleyzer, J. Haas, S. Hagopian, V. Hagopian, M. Jenkins, K.F. Johnson, E. Prettnner, H. Prosper, S. Sekmen

Florida Institute of Technology, Melbourne, U.S.A.

M.M. Baarmand, S. Guragain, M. Hohlmann, H. Kalakhety, H. Mermerkaya, R. Ralich, I. Vodopyanov

University of Illinois at Chicago (UIC), Chicago, U.S.A.

B. Abelev, M.R. Adams, I.M. Anghel, L. Apanasevich, V.E. Bazterra, R.R. Betts, J. Callner, M.A. Castro, R. Cavanaugh, C. Dragoiu, E.J. Garcia-Solis, C.E. Gerber, D.J. Hofman, S. Khalatian, C. Mironov, E. Shabalina, A. Smoron, N. Varelas

The University of Iowa, Iowa City, U.S.A.

U. Akgun, E.A. Albayrak, A.S. Ayan, B. Bilki, R. Briggs, K. Cankocak³⁶, K. Chung, W. Clarida, P. Debbins, F. Duru, F.D. Ingram, C.K. Lae, E. McCliment, J.-P. Merlo, A. Mestvirishvili, M.J. Miller, A. Moeller, J. Nachtman, C.R. Newsom, E. Norbeck, J. Olson, Y. Onel, F. Ozok, J. Parsons, I. Schmidt, S. Sen, J. Wetzel, T. Yetkin, K. Yi

Johns Hopkins University, Baltimore, U.S.A.

B.A. Barnett, B. Blumenfeld, A. Bonato, C.Y. Chien, D. Fehling, G. Giurgiu, A.V. Gritsan, Z.J. Guo, P. Maksimovic, S. Rappoccio, M. Swartz, N.V. Tran, Y. Zhang

The University of Kansas, Lawrence, U.S.A.

P. Baringer, A. Bean, O. Grachov, M. Murray, V. Radicci, S. Sanders, J.S. Wood, V. Zhukova

Kansas State University, Manhattan, U.S.A.

D. Bandurin, T. Bolton, K. Kaadze, A. Liu, Y. Maravin, D. Onoprienko, I. Svintradze, Z. Wan

Lawrence Livermore National Laboratory, Livermore, U.S.A.

J. Gronberg, J. Hollar, D. Lange, D. Wright

University of Maryland, College Park, U.S.A.

D. Baden, R. Bard, M. Boutemour, S.C. Eno, D. Ferencek, N.J. Hadley, R.G. Kellogg, M. Kirn, S. Kunori, K. Rossato, P. Rumerio, F. Santanastasio, A. Skuja, J. Temple, M.B. Tonjes, S.C. Tonwar, T. Toole, E. Twedt

Massachusetts Institute of Technology, Cambridge, U.S.A.

B. Alver, G. Bauer, J. Bendavid, W. Busza, E. Butz, I.A. Cali, M. Chan, D. D'Enterria, P. Everaerts, G. Gomez Ceballos, K.A. Hahn, P. Harris, S. Jaditz, Y. Kim, M. Klute, Y.-J. Lee, W. Li, C. Loizides, T. Ma, M. Miller, S. Nahn, C. Paus, C. Roland, G. Roland, M. Rudolph, G. Stephans, K. Sumorok, K. Sung, S. Vaurynovich, E.A. Wenger, B. Wyslouch, S. Xie, Y. Yilmaz, A.S. Yoon

University of Minnesota, Minneapolis, U.S.A.

D. Bailleux, S.I. Cooper, P. Cushman, B. Dahmes, A. De Benedetti, A. Dolgoplov, P.R. Duderov, R. Egeland, G. Franzoni, J. Haupt, A. Inyakin³⁷, K. Klapoetke, Y. Kubota, J. Mans, N. Mirman, D. Petyt, V. Rekovic, R. Rusack, M. Schroeder, A. Singovsky, J. Zhang

University of Mississippi, University, U.S.A.

L.M. Cremaldi, R. Godang, R. Kroeger, L. Perera, R. Rahmat, D.A. Sanders, P. Sonnek, D. Summers

University of Nebraska-Lincoln, Lincoln, U.S.A.

K. Bloom, B. Bockelman, S. Bose, J. Butt, D.R. Claes, A. Dominguez, M. Eads, J. Keller, T. Kelly, I. Kravchenko, J. Lazo-Flores, C. Lundstedt, H. Malbouisson, S. Malik, G.R. Snow

State University of New York at Buffalo, Buffalo, U.S.A.

U. Baur, I. Iashvili, A. Kharchilava, A. Kumar, K. Smith, M. Strang

Northeastern University, Boston, U.S.A.

G. Alverson, E. Barberis, O. Boeriu, G. Eulisse, G. Govi, T. McCauley, Y. Musienko³⁸, S. Muzaffar, I. Osborne, T. Paul, S. Reucroft, J. Swain, L. Taylor, L. Tuura

Northwestern University, Evanston, U.S.A.

A. Anastassov, B. Gobbi, A. Kubik, R.A. Ofierzynski, A. Pozdnyakov, M. Schmitt, S. Stoynev, M. Velasco, S. Won

University of Notre Dame, Notre Dame, U.S.A.

L. Antonelli, D. Berry, M. Hildreth, C. Jessop, D.J. Karmgard, T. Kolberg, K. Lannon, S. Lynch, N. Marinelli, D.M. Morse, R. Ruchti, J. Slaunwhite, J. Warchol, M. Wayne

The Ohio State University, Columbus, U.S.A.

B. Bylsma, L.S. Durkin, J. Gilmore³⁹, J. Gu, P. Killewald, T.Y. Ling, G. Williams

Princeton University, Princeton, U.S.A.

N. Adam, E. Berry, P. Elmer, A. Garmash, D. Gerbaudo, V. Halyo, A. Hunt, J. Jones, E. Laird, D. Marlow, T. Medvedeva, M. Mooney, J. Olsen, P. Piroué, D. Stickland, C. Tully, J.S. Werner, T. Wildish, Z. Xie, A. Zuranski

University of Puerto Rico, Mayaguez, U.S.A.

J.G. Acosta, M. Bonnett Del Alamo, X.T. Huang, A. Lopez, H. Mendez, S. Oliveros, J.E. Ramirez Vargas, N. Santacruz, A. Zatzerklyany

Purdue University, West Lafayette, U.S.A.

E. Alagoz, E. Antillon, V.E. Barnes, G. Bolla, D. Bortoletto, A. Everett, A.F. Garfinkel, Z. Gecse, L. Gutay, N. Ippolito, M. Jones, O. Koybasi, A.T. Laasanen, N. Leonardo, C. Liu, V. Maroussov, P. Merkel, D.H. Miller, N. Neumeister, A. Sedov, I. Shipsey, H.D. Yoo, Y. Zheng

Purdue University Calumet, Hammond, U.S.A.

P. Jindal, N. Parashar

Rice University, Houston, U.S.A.

V. Cuplov, K.M. Ecklund, F.J.M. Geurts, J.H. Liu, D. Maronde, M. Matveev, B.P. Padley, R. Redjimi, J. Roberts, L. Sabbatini, A. Tumanov

University of Rochester, Rochester, U.S.A.

B. Betchart, A. Bodek, H. Budd, Y.S. Chung, P. de Barbaro, R. Demina, H. Flacher, Y. Gotra, A. Harel, S. Korjenevski, D.C. Miner, D. Orbaker, G. Petrillo, D. Vishnevskiy, M. Zielinski

The Rockefeller University, New York, U.S.A.

A. Bhatti, L. Demortier, K. Goulios, K. Hatakeyama, G. Lungu, C. Mesropian, M. Yan

Rutgers, the State University of New Jersey, Piscataway, U.S.A.

O. Atramentov, E. Bartz, Y. Gershtein, E. Halkiadakis, D. Hits, A. Lath, K. Rose, S. Schnetzer, S. Somalwar, R. Stone, S. Thomas, T.L. Watts

University of Tennessee, Knoxville, U.S.A.

G. Cerizza, M. Hollingsworth, S. Spanier, Z.C. Yang, A. York

Texas A&M University, College Station, U.S.A.

J. Asaadi, A. Aurisano, R. Eusebi, A. Golyash, A. Gurrola, T. Kamon, C.N. Nguyen, J. Pivarski, A. Safonov, S. Sengupta, D. Toback, M. Weinberger

Texas Tech University, Lubbock, U.S.A.

N. Akchurin, L. Berntzon, K. Gumus, C. Jeong, H. Kim, S.W. Lee, S. Popescu, Y. Roh, A. Sill, I. Volobouev, E. Washington, R. Wigmans, E. Yazgan

Vanderbilt University, Nashville, U.S.A.

D. Engh, C. Florez, W. Johns, S. Pathak, P. Sheldon

University of Virginia, Charlottesville, U.S.A.

D. Andelin, M.W. Arenton, M. Balazs, S. Boutle, M. Buehler, S. Conetti, B. Cox, R. Hirosky, A. Ledovskoy, C. Neu, D. Phillips II, M. Ronquest, R. Yohay

Wayne State University, Detroit, U.S.A.

S. Gollapinni, K. Gunthoti, R. Harr, P.E. Karchin, M. Mattson, A. Sakharov

University of Wisconsin, Madison, U.S.A.

M. Anderson, M. Bachtis, J.N. Bellinger, D. Carlsmith, I. Crotty¹, S. Dasu, S. Dutta, J. Efron, F. Feyzi, K. Flood, L. Gray, K.S. Grogg, M. Grothe, R. Hall-Wilton¹, M. Jaworski, P. Klabbers, J. Klukas, A. Lanaro, C. Lazaridis, J. Leonard, R. Loveless, M. Magrans de Abril, A. Mohapatra, G. Ott, G. Polese, D. Reeder, A. Savin, W.H. Smith, A. Sourkov⁴⁰, J. Swanson, M. Weinberg, D. Wenman, M. Wensveen, A. White

†: Deceased

- 1: Also at CERN, European Organization for Nuclear Research, Geneva, Switzerland
- 2: Also at Universidade Federal do ABC, Santo Andre, Brazil
- 3: Also at Soltan Institute for Nuclear Studies, Warsaw, Poland
- 4: Also at Université de Haute-Alsace, Mulhouse, France
- 5: Also at Centre de Calcul de l'Institut National de Physique Nucleaire et de Physique des Particules (IN2P3), Villeurbanne, France
- 6: Also at Moscow State University, Moscow, Russia
- 7: Also at Institute of Nuclear Research ATOMKI, Debrecen, Hungary
- 8: Also at University of California, San Diego, La Jolla, U.S.A.
- 9: Also at Tata Institute of Fundamental Research - HECR, Mumbai, India
- 10: Also at University of Visva-Bharati, Santiniketan, India
- 11: Also at Facolta' Ingegneria Universita' di Roma "La Sapienza", Roma, Italy
- 12: Also at Università della Basilicata, Potenza, Italy
- 13: Also at Laboratori Nazionali di Legnaro dell' INFN, Legnaro, Italy
- 14: Also at Università di Trento, Trento, Italy
- 15: Also at ENEA - Casaccia Research Center, S. Maria di Galeria, Italy
- 16: Also at Warsaw University of Technology, Institute of Electronic Systems, Warsaw, Poland
- 17: Also at California Institute of Technology, Pasadena, U.S.A.
- 18: Also at Faculty of Physics of University of Belgrade, Belgrade, Serbia
- 19: Also at Laboratoire Leprince-Ringuet, Ecole Polytechnique, IN2P3-CNRS, Palaiseau, France
- 20: Also at Alstom Contracting, Geneve, Switzerland
- 21: Also at Scuola Normale e Sezione dell' INFN, Pisa, Italy
- 22: Also at University of Athens, Athens, Greece
- 23: Also at The University of Kansas, Lawrence, U.S.A.
- 24: Also at Institute for Theoretical and Experimental Physics, Moscow, Russia
- 25: Also at Paul Scherrer Institut, Villigen, Switzerland
- 26: Also at Vinca Institute of Nuclear Sciences, Belgrade, Serbia
- 27: Also at University of Wisconsin, Madison, U.S.A.
- 28: Also at Mersin University, Mersin, Turkey
- 29: Also at Izmir Institute of Technology, Izmir, Turkey
- 30: Also at Kafkas University, Kars, Turkey
- 31: Also at Suleyman Demirel University, Isparta, Turkey
- 32: Also at Ege University, Izmir, Turkey

- 33: Also at Rutherford Appleton Laboratory, Didcot, United Kingdom
- 34: Also at INFN Sezione di Perugia; Universita di Perugia, Perugia, Italy
- 35: Also at KFKI Research Institute for Particle and Nuclear Physics, Budapest, Hungary
- 36: Also at Istanbul Technical University, Istanbul, Turkey
- 37: Also at University of Minnesota, Minneapolis, U.S.A.
- 38: Also at Institute for Nuclear Research, Moscow, Russia
- 39: Also at Texas A&M University, College Station, U.S.A.
- 40: Also at State Research Center of Russian Federation, Institute for High Energy Physics, Protvino, Russia